Chapter 5
FORMULATION OF A 1-DIMENSIONAL / 3-DIMENSIONAL RATE-DEPENDENT CONSTITUTIVE MODEL FOR CHALK AND SOFT ROCK

INTRODUCTION

The time-dependent and rate-dependent behavior of geomaterials significantly influences their stress-strain response. Experimental programs have shown repeatedly that the material behavior of clays, sands, and soft rocks depends on loading rate (Bjerrum, 1967; Sallfors, 1975; Vaid and Campanella, 1977; Graham et al., 1983; Leroueil et al., 1985; Tatsuoka et al., 1999; Hayano et al., 2001). Apparent shear strength increases as loading rate increases.

Various constitutive models have been developed in an effort to simulate this time- and rate-dependent behavior. Bjerrum (1967) used the concept of equivalent age to predict the response of soft Norwegian clays. This model is based on the existence of time-lines, which are described in more detail in a later section. Other researchers, notably Yin and Graham (1989, 1994, 1999), Gutierrez (1999), and Yin et al. (2002) have also used the time-lines concept. Helm (1987) developed one-dimensional analytical solutions for consolidation using a poroviscosity model which is based on the same concept as the time-lines model. Shao et al. (2003) developed a time-dependent creep model for rock based on the concept of material degradation.

A similar approach to the original time-lines model was used in forming a rate-lines model, originally proposed by Vaid and Campanella (1977). Another model which simulates time-dependent behavior is the three-component model originally proposed by diBenedetto (1987). While other time-dependent models are based solely on strain decomposition, the three-component model refers to the existence of three stress components: these include one reversible component, one irreversible inviscid component, and one irreversible viscous component. This "isotach" model is based on lines of equal deformation rate. Two versions of the three-component model have been recently proposed: these include the TESRA (temporary effects of strain rate and acceleration) model of Tatsuoka et al. (2000) and the viscous evanescent model of diBenedetto et al. (2001). The difference between these versions is that the effects of the viscous stress component decreases as time passes in the viscous evanescent model, but remains constant in the TESRA model. A generalized three-component model which can be generalized to both versions is described by diBenedetto et al. (2002).

Many aspects of the rate-dependent models for clays may be used to describe rate-dependent behavior of soft rock. Rate-independent volumetric yield behavior of clays is typically described by an elliptical cap such as Modified Cam-Clay (Roscoe and Burland, 1968). Similarly, rate-independent volumetric yielding in chalk and other soft rocks is usually described by an elliptical cap (DeGennaro et al., 2003; Homand and Shao, 2000; Gutierrez, 1998). Therefore, the one-dimensional rate-dependent model may be extended for three-dimensional analysis for soft rocks using the same logic as is used for clays.

ONE-DIMENSIONAL MODEL FORMULATION

The assumption has long existed in the modeling of time-dependent behavior of geomaterials that deformation during compression includes both an "instant" and "delayed" component (Bjerrum, 1967). In this context, the instant component of deformation occurs due to application of external loads while the delayed component only occurs due to the passage of time.

Rate-independent elastoplastic models are based on the assumption that incremental strains can be decomposed into their reversible and irreversible, or elastic and plastic, components. The addition of time-dependent deformations to form an elastoviscoplastic constitutive model has been treated several ways by different researchers. Most commonly (Zienkiewicz and Cormeau, 1974; Desai and Zhang, 1987), the strain rate is divided into its reversible and irreversible, or elastic and viscoplastic, components. Other researchers (Borja and Kavazanjian, 1985; Kaliakin and Dafalias, 1990) have subdivided the irreversible component such that the strain rate consists of elastic, plastic, and time-dependent components. As stated earlier, experimental results from rate-dependent tests indicates that such a linear decomposition of the irreversible strain rate is not possible unless there is a coupling interaction between these two irreversible components. Since the irreversible strain components must be coupled to properly describe behavior of geomaterials using the three-component formulation, the decomposition of irreversible strains into plastic and time-dependent components complicates the formulation of the model without changing its results. Therefore, the strain rate on which this model is based uses the two-component assumption:

$$\dot{\varepsilon}_{ij} = \dot{\varepsilon}_{ij}^{r} + \dot{\varepsilon}_{ij}^{ir} = \dot{\varepsilon}_{ij}^{e} + \dot{\varepsilon}_{ij}^{vp} \tag{5.1}$$

where the superscripts *r*, *ir*, *e*, and *vp* indicate reversible, irreversible, elastic, and viscoplastic behavior, respectively. The reversible or elastic strain rate is calculated as a function of stress rate $\dot{\sigma}$:

$$\dot{\varepsilon}_{ij}^{e} = C_{ijkl}^{e}\dot{\sigma}_{kl} \tag{5.2}$$

where C_{ijkl}^{e} is the elastic compliance matrix. For a simplified one-dimensional case where only mean stress *p* and volumetric strain ε_v are considered, equation (5.2) simplifies to:

$$\dot{\varepsilon}_{v}^{e} = \frac{\dot{p}}{K} \tag{5.3}$$

where *K* is the bulk modulus.

Inelastic volumetric strain rate is calculated as a function of creep parameter ψ and volumetric age t_v using the volumetric creep law of Taylor (1948):

$$\dot{\varepsilon}_{v}^{vp} = \frac{\psi}{(1+e)}\frac{1}{t_v} \tag{5.4}$$

where *e* is the void ratio. The model is formulated using a modified time-lines approach. The time-lines model has the basis that lines of equal volumetric age exist in *e*-ln *p* space. The main components to the basic time-lines model are shown in Figure 5.1. Volumetric age is calculated using Bjerrum's (1967) assumption that all time-lines are linear, parallel, and oriented at slope λ (*i.e.*, same as the virgin compression line from conventional consolidation tests) in *e*-ln *p* space. Equally spaced time-lines in *e*-ln *p* space have volumetric ages that vary exponentially. The reference time-line (Yin and Graham, 1989; 1994; 1999) is defined such that the volumetric age for this time-line is the minimum volumetric age $t_{v,min}$ possible in the model. The preconsolidation stress p_c always lies on the reference time-line. The volumetric age of a sample is calculated relative to $t_{v,min}$, as shown by Borja and Kavazanjian (1985):

$$t_v = t_{v,\min}\left(\frac{p_c}{p}\right)^{\frac{\lambda-\kappa}{\psi}} \tag{5.5}$$

Several other assumptions are inherent in the model formulation. First, all instant compression lines or "instant time-lines" (Yin and Graham, 1989; 1994; 1999) are linear, parallel, and

oriented at slope κ in *e*-ln *p* space. Second, volumetric age increases linearly with time during creep loading ($\Delta t_v = \Delta t$ when $\dot{p} = 0$).

Each instant compression line corresponds to a different preconsolidation stress. During loading which involves passage of time, the stress point moves from one instant compression line to another such that p_c always increases in time.

One criticism of the linear time-lines model is that when equation (5.4) is integrated and time is infinite, creep strain becomes infinite. Then the total volume, and consequently the solid volume, of a geomaterial is reduced to zero. This condition is of course not possible. Yin et al. (2002) obviate this difficulty by identifying a maximum possible volumetric creep strain and modifying equation (5.4) such that all viscoplastic creep strains are calculated relative to the maximum. In their formulation, then, the creep function in fact becomes hyperbolic, asymptotically approaching the maximum creep strain. However, mechanical loading can still cause infinite volumetric strain and negative void ratio due to the linearity of the *e*-ln *p* relation. The model proposed here is modified from the basic time-lines model in that the reference time-line, and therefore the *e*-ln *p* relation, is nonlinear. This is accomplished by making the compression coefficient λ a function of void ratio:

$$\lambda = \lambda_0 \left(\frac{e}{N} \right)^A \tag{5.6}$$

The reference time-line is anchored in *e*-ln *p* space at the void ratio *N* when $p = 1$. The reference coefficient λ_0 is then the value of λ at $p = 1$, and the coefficient *A* affects the nonlinearity of the *e*-ln *p* relation. The equation of the reference time-line is

$$p = p_c = \exp\left(\frac{N - e}{\lambda} \right) \tag{5.7}$$

so it is apparent that λ is a secant slope between $p = 1$ and the stress of interest. The effects of the parameter *A* on the value of λ and on the reference time-line in *e*-ln *p* space are shown in Figure 5.2. It may be seen that the nonlinearity of the reference time-line is only significant for relatively large values of *A*, and only at high stresses as the void ratio approaches zero.

Elasticity in chalk and other soft rocks appears to be linear rather than pressure-dependent. Therefore, the base model must also be modified to reflect this behavior. The instant

time-lines for a model with linear elasticity are not linear in *e*-ln *p* space, but instead are curved. However, all instant time-lines have the same slope for a given mean stress.

Equations (5.1), (5.3), and (5.4) can then be used to simulate the rate-dependent behavior of geomaterials as described in the following section.

STRESS-RATE CONTROL AND STRAIN-RATE CONTROL

Constitutive equations are generally presented in either stress-rate controlled or strain-rate controlled form. When the constitutive behavior of a geomaterial is sought, laboratory tests are performed, usually under either stress-rate controlled or strain-rate controlled conditions. Some laboratory tests have mixed control (*i.e.*, a mixture of stress-rate controlled components and strain-rate controlled components); in these cases, constitutive behavior can only be simulated using finite element simulations. Stress-rate controlled and strain-rate controlled constitutive equations for the proposed rate-dependent model are presented in this section.

For stress-rate controlled conditions in one dimension, the governing constitutive equation is obtained by substituting equations (5.3) and (5.4) into the one-dimensional form of equation (5.1):

$$\dot{\varepsilon}_v = \frac{\dot{p}}{K} + \frac{\psi}{(1+e)}\frac{1}{t_v} \tag{5.8}$$

Creep loading is a special type of stress-controlled loading in which certain stress components remain constant with respect to time (in one dimension, $\dot{p} = 0$). For creep loading, equation (5.8) simplifies to:

$$\dot{\varepsilon}_v = \frac{\psi}{(1+e)}\frac{1}{t_v} \tag{5.9}$$

The governing constitutive equation for strain-rate controlled loading is obtained by substituting equations (5.3) and (5.4) into the rearranged one-dimensional form of equation (5.1):

$$\dot{p} = K\left(\dot{\varepsilon}_v - \frac{\psi}{(1+e)}\frac{1}{t_v}\right) \tag{5.10}$$

Stress-relaxation loading is a special type of strain-controlled loading in which certain strain components remain constant with respect to time (in one dimension, $\dot{\varepsilon}_v = 0$). For stress-relaxation loading, equation (5.10) simplifies to:

$$\dot{p} = -K \frac{\psi}{(1+e)} \frac{1}{t_v} \tag{5.11}$$

The preconsolidation stress also increases as the inelastic strain accumulates. Borja and Kavazanjian (1985) showed that the rate of increase of p_c with respect to inelastic strain is:

$$\frac{\partial p_c}{\partial \varepsilon_v^{vp}} = \frac{1+e}{\lambda - \kappa} p_c \tag{5.12}$$

Then the time rate of increase in p_c may be obtained:

$$\dot{p}_c = \frac{\partial p_c}{\partial \varepsilon_v^{vp}} \frac{\partial \varepsilon_v^{vp}}{\partial t} = \frac{\psi}{\lambda - \kappa} \frac{p_c}{t_v} \tag{5.13}$$

Integration of the rate-dependent constitutive equations for use in numerical simulations is discussed in the next section.

INTEGRATION OF RATE-DEPENDENT CONSTITUTIVE EQUATIONS

The integrated forms of equations (5.8), (5.10), and (5.13), respectively, are:

$$\Delta \varepsilon_v = \int_{p_0}^{p_f} \frac{dp}{K} + \int_{t_0}^{t_f} \frac{\psi}{(1+e)} \frac{dt}{t_v} \tag{5.14}$$

$$\Delta p = \int_{\varepsilon_{v0}}^{\varepsilon_{vf}} K \, d\varepsilon_v - \int_{t_0}^{t_f} K \frac{\psi}{(1+e)} \frac{dt}{t_v} \tag{5.15}$$

$$\Delta p_c = \int_{t_{v0}}^{t_{vf}} \frac{\psi}{\lambda - \kappa} \frac{p_c}{t_v} dt \tag{5.16}$$

The subscripts 0 and *f* indicate the specified values at the beginning and end of the loading step, respectively. Completing the integration for equations (5.14)-(5.16) for a loading step of finite duration is difficult, similar to the problem for a plastic loading step in classical elastoplasticity, because the volumetric age t_v that appears in the second term of all three equations changes

throughout the loading step. For nonlinear elastic models, the bulk modulus K also changes throughout the loading step. Similar to the integration problem in classical elastoplasticity, evaluation of the varying quantities at different points throughout the loading interval leads to different solutions.

There is a major difference between integration of rate-independent elastoplastic relations and rate-dependent inelastic relations in that for many integration schemes in time-independent elastoplasticity, the goal of the integration procedure is to find values of the final stress point and final hardening parameter that satisfy the consistency condition such that the stress point lies on the yield surface ($f = 0$, where f is the yield function). Such a well-defined criterion does not exist to determine that a "correct" integration of rate-dependent elastic relations has been performed. For the rate-independent problem, a poor integration procedure may lead to non-convergence and failure to reach a solution. For the time-independent problem, a solution should be obtained in general since no criterion such as the consistency condition exists to render a possible solution improper or to state that requirements for a solution have not been met.

The strain rate is assumed to be constant throughout the loading step. It is assumed here that for a given loading step, the duration and stress rate or strain rate is specified. For stress-rate controlled loading, the stress increment is then the product of the stress rate and the duration; the same logic applies to strain-rate controlled loading.

Integration of the first term in equations (5.14)-(5.15) may be completed analytically for linear elastic models because the limits of integration are known and all other terms in the integral (*i.e.*, bulk modulus) are constant:

$$\Delta\varepsilon_v = \frac{p}{K}\bigg|_{p_0}^{p_f} + \int_{t_0}^{t_f} \frac{\psi}{(1+e)}\frac{dt}{t_v} = \frac{\Delta p}{K} + \int_{t_0}^{t_f} \dot{\varepsilon}_v^{vp}\, dt \tag{5.17}$$

$$\Delta p = K\varepsilon_v\big|_{\varepsilon_{v0}}^{\varepsilon_{vf}} - \int_{t_0}^{t_f} K\frac{\psi}{(1+e)}\frac{dt}{t_v} = K\Delta\varepsilon_v - \int_{t_0}^{t_f} K\dot{\varepsilon}_v^{vp}\, dt \tag{5.18}$$

Nonlinear elastic models often use the pressure-dependent bulk modulus of Cam-Clay:

$$K = \frac{(1+e)p}{\kappa} \tag{5.19}$$

For this nonlinear elastic model, the first term in equation (5.14) may be integrated analytically assuming that the change in void ratio is small:

$$\Delta\varepsilon_v = \int_{p_0}^{p_f} \frac{\kappa}{1+e}\frac{dp}{p} + \int_{t_0}^{t_f} \frac{\psi}{(1+e)}\frac{dt}{t_v} = \frac{\kappa}{1+e_0}\ln\left(1+\frac{\Delta p}{p}\right) + \int_{t_0}^{t_f} \dot{\varepsilon}_v^{vp}\, dt \tag{5.20}$$

The same assumption is required to integrate the strain-rate controlled constitutive equation analytically for this nonlinear elastic model. The rate equation (5.10) is simplified to:

$$\frac{dp}{p} = \frac{1+e}{\kappa}\left(d\varepsilon_v - \dot{\varepsilon}_v^{ir}\, dt\right) = \frac{1+e}{\kappa} d\varepsilon_v - \frac{\psi}{\kappa}\frac{dt}{t_v} \tag{5.21}$$

which may be integrated and simplified as follows:

$$\Delta p = p_0\left[\exp\left(\frac{1+e_0}{\kappa}\Delta\varepsilon_v - \int_{t_0}^{t_f}\frac{1+e}{\kappa}\dot{\varepsilon}_v^{vp}\, dt\right) - 1\right] \tag{5.22}$$

Even though parts of equations (5.14) and (5.15) may be integrated analytically for certain elastic models, numerical integration procedures must be used to find a complete solution to these equations. Several different integration procedures for the second term are described in the following paragraphs. These solution procedures include the explicit Euler method, higher-order explicit methods including the fourth-order Runge-Kutta method, the secant age method, and the creep solution (*i.e.*, exact solution for creep).

Explicit Euler Method

Integration using the Euler or first-order explicit method uses the time-dependent strain rate and therefore the volumetric age t_{v0} at the start of the loading interval. The viscoplastic strain increment and preconsolidation stress increment are then:

$$\Delta\varepsilon_v^{vp} = \int_{t_{v0}}^{t_{vf}} \dot{\varepsilon}_v^{vp}\, dt = \left(\dot{\varepsilon}_v^{vp}\right)_0 \Delta t = \frac{\psi}{1+e_0}\frac{\Delta t}{t_{v0}} \tag{5.23}$$

$$\Delta p_c = \int_{t_{v0}}^{t_{vf}} \frac{\psi}{\lambda-\kappa}\frac{p_c}{t_v} dt = \frac{\psi}{\lambda-\kappa}\frac{p_c}{t_{v0}}\Delta t \tag{5.24}$$

This method therefore has the inherent assumption that the volumetric age does not change throughout the loading interval. Error is introduced if the volumetric age does indeed change during a given loading step. Since the volumetric age does change during a general loading step, this error may be considerable.

Higher-Order Explicit Methods

Higher-order explicit methods use additional terms of the Taylor expansion and therefore require higher-order derivatives to calculate solutions. Some numerical methods have been developed which attain the same accuracy as higher-order explicit methods but require only first-order derivatives; such methods require multiple function evaluations and include the modified Euler method and the Runge-Kutta methods.

The modified Euler method and fourth-order Runge-Kutta method are both based on using a weighted average time-dependent strain rate over the loading interval:

$$\left(\dot{\varepsilon}_v^{vp}\right)_{avg} = \sum_1^n w_n \left(\dot{\varepsilon}_v^{vp}\right)_n \tag{5.25}$$

where n is the number of function evaluations required and w is the set of weighting function associated with the points of function evaluation. For the modified Euler method, $n = 2$ and $w = \{1/2,1/2\}$; for the fourth-order Runge-Kutta method, $n = 4$ and $w = \{1/6,1/3,1/3,1/6\}$. The use of both of these methods is described by Sloan (1987) for rate-independent elastoplasticity. A slightly different method is used here for rate-dependent inelasticity. The use of the second-order modified Euler method is described in detail for a strain-rate controlled loading step as follows. A linear elastic model is used for this illustrative example.

For strain-rate controlled loading, the duration Δt and strain rate $\dot{\varepsilon}_v$ are specified; the strain increment $\Delta\varepsilon_v$ for the step is then calculated as described above. The initial stress and preconsolidation stress are p_0 and $p_{c,0}$, respectively, while the initial volumetric age is t_{v0}. The stress increment Δp and preconsolidation stress increment Δp_c are calculated as for the explicit Euler method:

$$\Delta p_1 = K\Delta\varepsilon_v - K\frac{\psi}{1+e_0}\frac{\Delta t}{t_{v0}} \tag{5.26}$$

$$\Delta p_{c,1} = \frac{\psi}{\lambda - \kappa} \frac{p_c}{t_{v0}} \Delta t \tag{5.27}$$

Next, these variables are updated and the new volumetric age is calculated (for nonlinear models, the coefficients λ and κ must be updated before the volumetric age is calculated):

$$p_1 = p_0 + \Delta p_1 \tag{5.28}$$

$$p_{c,1} = p_{c,0} + \Delta p_{c,1} \tag{5.29}$$

$$t_{v1} = t_{v,\min} \left(\frac{p_{c,1}}{p_1} \right)^{\frac{\lambda - \kappa}{\psi}} \tag{5.30}$$

A second stress increment and preconsolidation stress increment are calculated for an equal strain increment and time increment, using the Explicit Euler equations:

$$\Delta p_2 = K \Delta \varepsilon_v - K \frac{\psi}{1 + e_0} \frac{\Delta t}{t_{v1}} \tag{5.31}$$

$$\Delta p_{c,2} = \frac{\psi}{\lambda - \kappa} \frac{p_{c,1}}{t_{v1}} \Delta t \tag{5.32}$$

The final updated stress increment and preconsolidation stress increment is equal to one-half the sum of both increments:

$$p_f = p_0 + \frac{\left(\Delta p_1 + \Delta p_2 \right)}{2} \tag{5.33}$$

$$p_{c,f} = p_{c,0} + \frac{\left(\Delta p_{c,1} + \Delta p_{c,2} \right)}{2} \tag{5.34}$$

A similar multistep approach may be implemented using the rules for the fourth-order Runge-Kutta method. It can be verified that higher-order explicit methods yield more accurate answers than the explicit Euler method. As for the integration of rate-independent constitutive equations using higher-order explicit methods, it is possible to estimate the maximum error for a given loading step and to use a substepping procedure to control the error.

Secant Age Method

The secant age method described here is an application of the generalized trapezoidal rule. For the secant method, the average volumetric age of the sample over a given loading interval is used to calculate the time-dependent strain rate. Like other applications of the generalized trapezoidal rule, the secant method requires iteration to obtain a converged solution. The iterative procedure is described below for a strain-rate controlled loading step.

The first estimate for the stress increment and preconsolidation stress may be obtained using any method. The preconsolidation stress is then calculated to be consistent with the strain increment and resulting final void ratio using a modified form of equation (5.7),

$$p_c = \exp\left[\frac{N - e_f + \kappa \ln\left(p_c / p\right)}{\lambda}\right] = \exp\left[\frac{N - e_f + \frac{\kappa\psi}{\lambda - \kappa}\ln\left(t_v / t_{v,\min}\right)}{\lambda}\right] \tag{5.35}$$

In equation (5.35), the final void ratio is determined by using the following conversions between volumetric strain and void ratio:

$$e_f = \frac{1 + e_0}{\exp\left(\Delta\varepsilon_v\right)} - 1 \tag{5.36a}$$

$$\Delta\varepsilon_v = \ln\left(\frac{1 + e_0}{1 + e_f}\right) \tag{5.36b}$$

The volumetric age t_{vf} of the sample at the end of the loading step is then determined. The average or secant volumetric age $\bar{t}_v$ for the sample is then calculated; since the volumetric age lines are spaced equally for exponentially changing volumetric ages, the logarithmic average (or square root) of the initial and final volumetric age is considered to be the average volumetric age of a sample for a given loading step.

$$\bar{t}_v = \sqrt{t_{v0} t_{vf}} \tag{5.37}$$

The residual r between the estimated final stress and the final stress corresponding to the secant volumetric age is then calculated:

$$r = p - \left(p_0 + K\Delta\varepsilon_v - K\frac{\psi}{(1+e_f)}\frac{\Delta t}{\bar{t}_v} \right) \tag{5.38}$$

The increment to the final volumetric age is determined using Newton-Raphson iteration, as follows:

$$\Delta t_{vf} = \frac{-r}{\partial r / \partial t_{vf}} \tag{5.39}$$

In equation (5.39), the value of $\partial r / \partial t_{vf}$ is given as follows:

$$\frac{\partial r}{\partial t_{vf}} = -K\frac{\psi}{(1+e_f)}\frac{\Delta t}{\bar{t}_v^2}\frac{\partial \bar{t}_v}{\partial t_{vf}} - \frac{p}{t_{vf}}\frac{\psi}{(\lambda-\kappa)} = -\frac{K}{2}\frac{\psi}{(1+e_f)}\frac{\Delta t}{\bar{t}_v^2}\sqrt{\frac{t_{v0}}{t_{vf}}} + \frac{p}{t_{vf}}\frac{\psi}{(\kappa-\lambda)} \tag{5.40}$$

The final volumetric age is changed by the increment Δt_{vf}, and the next iteration begins anew with equation (5.35). The iteration process continues until the residual r is reduced to zero, within a prescribed tolerance.

Creep Solution

During creep loading, all stresses remain constant ($\dot{p} = 0$) as strain accumulates due to the passage of time. The soil ages linearly with clock time for this type of loading program. The incremental constitutive relation for this stress-controlled loading program comes from equation (5.9):

$$d\varepsilon_v = \frac{\psi}{1+e}\frac{dt}{t_v} \tag{5.41}$$

Since geomaterials age linearly with clock time, the incremental change in volumetric age is exactly equal to the duration of a given loading step, or $\Delta t_v = \Delta t$. Integration of equation (5.41) can then be performed analytically, assuming that the change in void ratio is small:

$$\Delta\varepsilon_v = \frac{\psi}{1+e}\ln\left(\frac{t_{v0}+\Delta t}{t_{v0}}\right) = \frac{\psi}{1+e}\ln\left(1+\frac{\Delta t}{t_{v0}}\right) \tag{5.42}$$

The increment in preconsolidation stress is calculated in the same way:

$$\Delta p_c = p_c \frac{\psi}{\lambda - \kappa} \ln\left(1 + \frac{\Delta t}{t_{v0}}\right) \tag{5.43}$$

It should be noted that the change in volumetric age is not equal to the time change for general loading conditions. This solution then introduces error for a general loading step. Also, for the nonlinear *e*-ln *p* model proposed here, some error is introduced even for creep loading because the coefficient λ changes as creep progresses. Therefore, even though geomaterials age linearly with clock time, the nonlinearity of λ must be accounted for to obtain an accurate solution.

Comparison of Integration Methods

The integration methods described above will be implemented and their results compared for two single-step one-dimensional simulations, including creep and stress relaxation. The results will be compared to "exact" solutions which are obtained for the same loading program subdivided into 500 smaller steps. In both cases, the initial stress point lies on the reference time-line. Material properties and initial conditions for the simulated geomaterial are shown in Table 5.1. Elasticity for the simulated geomaterial is assumed to be linear.

The first example simulates creep loading for 5 days. The second example simulates stress relaxation loading for 1 day. The results for the simulations are shown in Tables 5.2 and 5.3. As seen, all methods have some error associated with their solutions. For the creep loading program, the creep solution is the most accurate. This solution has only a very slight error in strain increment associated with the change is void ratio, and a larger error for the change in preconsolidation stress. The errors in the solutions for other methods range from slight to substantial. All methods have errors for the stress relaxation loading program. However, the average error for the secant age method is much less than that for any other method.

EXTENSION TO THREE-DIMENSIONAL BEHAVIOR

The proposed rate-dependent constitutive model must be extended to simulate three-dimensional loading conditions in order to be useful for real geotechnical problems. The proposed model is extended to 3-D conditions using a similar approach to the "volumetric scaling" approach of Borja and Kavazanjian (1985). This method determines all viscoplastic strain-rate components by scaling these against the viscoplastic volumetric strain-rate:

$$\dot{\varepsilon}_{ij}^{vp} = \dot{\varepsilon}_{v}^{vp} \frac{\partial \varepsilon_{ij}^{vp}}{\partial \varepsilon_{v}^{vp}} = \frac{\psi}{1+e_{eq}} \frac{1}{t_v} \frac{\partial g / \partial \sigma_{ij}}{\partial g / \partial p} \tag{5.44}$$

In equation (5.44), g is the viscoplastic potential for the model and e_{eq} is the equivalent void ratio. For this model, a generalized form of the elliptical cap surface of Modified Cam-Clay, introduced by Gutierrez (1998), is used as the viscoplastic potential in p-q space. This surface is shown in Figure 5.3a. In the triaxial compression plane ($\sigma_1 > \sigma_2 = \sigma_3$), the equation for the viscoplastic potential surface is:

$$\begin{aligned} g &= q^2 - M^2 R^2 p_{eq}^2 + M^2 R^2 \frac{\left(p - R p_{eq}\right)^2}{\left(1-R\right)^2} \\ &= q^2 - M^2 R^2 p_{eq}^2 + M_2^2 R^2 \left(p - R p_{eq}\right)^2 \end{aligned} \tag{5.45}$$

where M is the slope that controls the position of the viscoplastic potential surface in p-q space; R is the parameter that controls the aspect ratio of the viscoplastic potential surface; M_2 ($=\frac{MR}{1-R}$) is the aspect ratio of the viscoplastic potential surface in p-q space; and p_{eq} (Stolle et al., 1999) is the equivalent hydrostatic stress on the viscoplastic potential surface. The volumetric age is equal at any point on a single viscoplastic potential surface. Therefore, the time-lines model in the p-e plane appears as shown in Figure 5.1 except that the axes are replaced by p_{eq} and e_{eq}. In p-q space, the rate lines model appears as shown in Figure 5.4a. The physical meanings of p_{eq} and e_{eq} are indicated in Figure 5.4b where the relevant components of the rate-dependent model are shown in p-q-e space.

As is typical of constitutive models for geomaterials, strength is a function of intermediate principal stress or of Lode angle θ. The William-Warnke (1975) surface, a third-invariant model that resembles the Mohr-Coulomb model but has a smooth surface in the π-plane (Figure 5.3b), is used to represent the third-invariant behavior of this constitutive model. The third-invariant dependence using the William-Warnke surface appears as the function G_θ, which scales the aspect ratio of the elliptical viscoplastic potential surface in the π-plane:

$$g = q^2 - G_\theta^2 M^2 R^2 p_{eq}^2 + G_\theta^2 M_2^2 \left(p - R p_{eq}\right)^2 \tag{5.46}$$

For triaxial compression conditions, G_θ equals its maximum value of 1, while for triaxial extension conditions, G_θ equals its minimum value of k. For other intermediate principal stress conditions, G_θ lies somewhere between these extremes; see Figure 5.3b.

The volumetric age controls the viscoplastic strain rate in the 3-D formulation in the same way as it does for the 1-D formulation described earlier. The difference for the 3-D formulation is that instead of the mean stress p, the equivalent hydrostatic stress p_{eq} is used to calculate the volumetric age:

$$t_v = t_{v,\min}\left(\frac{p_c}{p_{eq}}\right)^{\frac{\lambda-\kappa}{\psi}} \tag{5.47}$$

The equivalent mean stress p_{eq} is the isotropic stress state corresponding to the actual stress state, and the equivalent void ratio is the void ratio for the equivalent mean stress. For a given stress state, the value of p_{eq} may be found by setting equation (5.46) equal to zero and rearranging:

$$p_{eq} = \frac{G_\theta M_2^2 p - \sqrt{G_\theta^2 M^2 M_2^2 p^2 + q^2\left(M^2 - M_2^2\right)}}{G_\theta R\left(M_2^2 - M^2\right)} \tag{5.48}$$

Mathematically, e_{eq} is defined using a modified form of equation (5.36a) as follows:

$$e_{eq} = \frac{1+e}{\exp\left(\frac{p_{eq}-p}{K}\right)} - 1 \tag{5.49}$$

For $R = 0.5$, the viscoplastic potential surface simplifies to that of Modified Cam-Clay, and equations (5.45), (5.46), and (5.48) simplify to the following expressions:

$$g = q^2 - M^2 p\left(p_{eq} - p\right) \tag{5.50}$$

$$g = q^2 - G_\theta^2 M^2 p\left(p_{eq} - p\right) \tag{5.51}$$

$$p_{eq} = p + \frac{q^2}{G_\theta^2 M^2 p} \tag{5.52}$$

Using the three-dimensional model, it is possible to formulate constitutive equations for general stress-rate controlled loadings or strain-rate controlled loadings. Under triaxial loading

conditions, it is possible to control two of the following four parameters: axial strain rate $\dot{\varepsilon}_a$, radial strain rate $\dot{\varepsilon}_r$, axial stress rate $\dot{\sigma}_a$, and radial stress rate $\dot{\sigma}_r$. The constitutive rate equations for stress-rate controlled loading conditions are:

$$\begin{aligned}\dot{\varepsilon}_a &= \frac{\dot{\sigma}_a}{E} - \frac{2\nu\dot{\sigma}_r}{E} + \frac{\psi}{(1+e)}\frac{1}{t_v}\frac{\partial g/\partial \sigma_a}{\partial g/\partial p} \\ &= \frac{\dot{\sigma}_a}{E} - \frac{2\nu\dot{\sigma}_r}{E} + \frac{\psi}{(1+e)}\frac{1}{t_v}\left(\frac{1}{3} + \frac{\partial g/\partial q}{\partial g/\partial p}\right)\end{aligned} \tag{5.53}$$

$$\begin{aligned}\dot{\varepsilon}_r &= \frac{-\nu\dot{\sigma}_a}{E} - \frac{(1-\nu)\dot{\sigma}_r}{E} + \frac{\psi}{(1+e)}\frac{1}{t_v}\frac{\partial g/\partial \sigma_r}{\partial g/\partial p} \\ &= \frac{-\nu\dot{\sigma}_a}{E} - \frac{(1-\nu)\dot{\sigma}_r}{E} + \frac{\psi}{(1+e)}\frac{1}{t_v}\left(\frac{1}{3} - \frac{1}{2}\frac{\partial g/\partial q}{\partial g/\partial p}\right)\end{aligned} \tag{5.54}$$

where E and ν are the elastic modulus and Poisson's ratio, respectively.

The rate equations for strain-rate controlled loading conditions are:

$$\begin{aligned}\dot{\sigma}_a &= \left(K + \tfrac{4}{3}G\right)\left(\dot{\varepsilon}_a - \frac{\psi}{(1+e)}\frac{1}{t_v}\frac{\partial g/\partial \sigma_a}{\partial g/\partial p}\right) + 2\left(K - \tfrac{2}{3}G\right)\left(\dot{\varepsilon}_r - \frac{\psi}{(1+e)}\frac{1}{t_v}\frac{\partial g/\partial \sigma_r}{\partial g/\partial p}\right) \\ &= \left(K + \tfrac{4}{3}G\right)\dot{\varepsilon}_a + 2\left(K - \tfrac{2}{3}G\right)\dot{\varepsilon}_r - K\frac{\psi}{(1+e)}\frac{1}{t_v} - 2G\frac{\psi}{(1+e)}\frac{1}{t_v}\frac{\partial g/\partial q}{\partial g/\partial p}\end{aligned} \tag{5.55}$$

$$\begin{aligned}\dot{\sigma}_r &= \left(K - \tfrac{2}{3}G\right)\left(\dot{\varepsilon}_a - \frac{\psi}{(1+e)}\frac{1}{t_v}\frac{\partial g/\partial \sigma_a}{\partial g/\partial p}\right) + 2\left(K + \tfrac{1}{3}G\right)\left(\dot{\varepsilon}_r - \frac{\psi}{(1+e)}\frac{1}{t_v}\frac{\partial g/\partial \sigma_r}{\partial g/\partial p}\right) \\ &= \left(K - \tfrac{2}{3}G\right)\dot{\varepsilon}_a + 2\left(K + \tfrac{1}{3}G\right)\dot{\varepsilon}_r - K\frac{\psi}{(1+e)}\frac{1}{t_v} + G\frac{\psi}{(1+e)}\frac{1}{t_v}\frac{\partial g/\partial q}{\partial g/\partial p}\end{aligned} \tag{5.56}$$

where G is the shear modulus.

Creep loading is generally performed under one of the following conditions: either (1) axial stress rate $\dot{\sigma}_a = 0$ and radial stress rate $\dot{\sigma}_r = 0$ throughout creep loading, or (2) axial stress rate $\dot{\sigma}_a = 0$ and radial strain rate $\dot{\varepsilon}_r = 0$ for the duration of creep loading. For case 1, the axial and radial strain rates may be solved by setting the stress rates equal to zero in equations (5.53) and (5.54):

$$\dot{\varepsilon}_a = \frac{\psi}{(1+e)}\frac{1}{t_v}\left(\frac{1}{3} + \frac{\partial g/\partial q}{\partial g/\partial p}\right) \tag{5.57}$$

$$\dot{\varepsilon}_r = \frac{\psi}{(1+e)} \frac{1}{t_v} \left(\frac{1}{3} - \frac{1}{2} \frac{\partial g / \partial q}{\partial g / \partial p} \right) \tag{5.58}$$

Wood (1990) showed that for Modified Cam-Clay under triaxial conditions (*i.e.*, $G_\theta = 1$),

$$\frac{\partial g / \partial q}{\partial g / \partial p} = \frac{2\eta}{M^2 - \eta^2} \tag{5.59}$$

where η (= q / p) is the shear stress ratio. A more complicated expression results for the generalized viscoplastic potential surface:

$$\frac{\partial g / \partial q}{\partial g / \partial p} = \frac{\eta \left(M_2^2 - M^2 \right)}{M_2^2 \left(\sqrt{M^2 M_2^2 + \eta^2 \left(M^2 - M_2^2 \right)} - M^2 \right)} \tag{5.60}$$

Substituting equation (5.59) or (5.60) into equations (5.57)-(5.58), we see that the relative strain rates depend only on the shear stress ratio η. For the simplified viscoplastic potential of Modified Cam-Clay (*i.e.*, $R = 0.5$), we obtain:

$$\dot{\varepsilon}_a = \frac{\psi}{(1+e)} \frac{1}{t_v} \left(\frac{1}{3} + \frac{2\eta}{M^2 - \eta^2} \right) \tag{5.61}$$

$$\dot{\varepsilon}_r = \frac{\psi}{(1+e)} \frac{1}{t_v} \left(\frac{1}{3} - \frac{\eta}{M^2 - \eta^2} \right) \tag{5.62}$$

Creep then proceeds under K_0 conditions (*i.e.*, no radial strain) for the following shear stress ratio:

$$\eta_{K_0} = \frac{\sqrt{9 + 4M^2}}{2} - \frac{3}{2} \tag{5.63}$$

Radial strain is contractive for shear stress ratios less than η_{K_0}, and is dilatant for greater shear stress ratios.

For creep case 2, the axial strain rate may be solved by setting the radial strain rate equal to zero, solving for $\dot{\sigma}_a$ in equation (5.54), and substituting the resulting expression into equation (5.53):

$$\dot{\varepsilon}_a = \frac{1}{(1-\nu)} \frac{\psi}{(1+e)} \frac{1}{t_v} \left[\frac{1+\nu}{3} + (1-2\nu) \frac{\partial g / \partial q}{\partial g / \partial p} \right] \tag{5.64}$$

The expression in equation (5.64) is then used in equation (5.56) to solve for the radial stress rate:

$$\dot{\sigma}_r = \frac{E}{(1-\nu)}\frac{\psi}{(1+e)}\frac{1}{t_v}\left[\frac{1}{2}\frac{\partial g/\partial q}{\partial g/\partial p} - \frac{1}{3}\right] \tag{5.65}$$

For $R = 0.5$, the axial strain rate and radial stress rate are simplified as follows:

$$\dot{\varepsilon}_a = \frac{1}{(1-\nu)}\frac{\psi}{(1+e)}\frac{1}{t_v}\left[\frac{1+\nu}{3} + (1-2\nu)\frac{2\eta}{M^2-\eta^2}\right] \tag{5.66}$$

$$\dot{\sigma}_r = \frac{E}{(1-\nu)}\frac{\psi}{(1+e)}\frac{1}{t_v}\left[\frac{\eta}{M^2-\eta^2} - \frac{1}{3}\right] \tag{5.67}$$

For $R = 0.5$, the radial stress rate is equal to zero for the shear stress ratio given in equation (5.63).

For stress-relaxation loading, all strain rates are equal to zero. The stress rates resulting from stress-relaxation loading are obtained by setting the strain rates in equations (5.55)-(5.56) equal to zero:

$$\dot{\sigma}_a = -K\frac{\psi}{(1+e)}\frac{1}{t_v} - 2G\frac{\psi}{(1+e)}\frac{1}{t_v}\frac{\partial g/\partial q}{\partial g/\partial p} \tag{5.68}$$

$$\dot{\sigma}_r = -K\frac{\psi}{(1+e)}\frac{1}{t_v} + G\frac{\psi}{(1+e)}\frac{1}{t_v}\frac{\partial g/\partial q}{\partial g/\partial p} \tag{5.69}$$

For $R = 0.5$, these expressions are simplified as follows:

$$\dot{\sigma}_a = -K\frac{\psi}{(1+e)}\frac{1}{t_v} - 4G\frac{\psi}{(1+e)}\frac{1}{t_v}\frac{\eta}{M^2-\eta^2} \tag{5.70}$$

$$\dot{\sigma}_r = -K\frac{\psi}{(1+e)}\frac{1}{t_v} + 2G\frac{\psi}{(1+e)}\frac{1}{t_v}\frac{\eta}{M^2-\eta^2} \tag{5.71}$$

For stress relaxation loading, the relative stress rates depend only on the shear stress ratio η. The radial stress rate equals zero for the following shear stress ratio:

$$\eta = \frac{\sqrt{9(1-2\nu)^2 + 4M^2(1+\nu)^2}}{2(1+\nu)} - \frac{3(1-2\nu)}{2(1+\nu)} \tag{5.72}$$

Radial stress decreases for lesser shear stress ratios, and increases for greater shear stress ratios.

Note that the strain rates in equations (5.61)-(5.62) and (5.66), the stress rates in equations (5.67) and (5.70)-(5.71), and the steady-state shear stress ratios in equations (5.63) and (5.72), apply only for $R = 0.5$. For $R \neq 0.5$, the general expressions for strain rates in equations (5.57)-(5.58) and (5.64), and for stress rates in equations (5.65) and (5.68)-(5.69) apply. These expressions can be used with the plastic flow direction given in equation (5.60) to obtain numerical solutions for the steady-state shear stress ratios in the general case for creep and stress relaxation.

SIMULATIONS AND RATE-DEPENDENT BEHAVIOR

Strain rate and/or stress rate strongly influence the behavior of geomaterials under compression. For strain-rate controlled hydrostatic compression conditions, the stress-strain behavior of a geomaterial under different strain rates was investigated. The material properties are the same as for the previous example (see Table 5.1), but starting conditions are different, as shown in Table 5.4. Results for strain-rate controlled loading are shown for several different constant strain rates in Figure 5.5. The equivalent graph for stress-rate controlled conditions is shown in Figure 5.6. It is clearly shown that more inelastic deformation accumulates under lesser stress states when a lesser strain rate or stress rate is applied. The apparent preconsolidation stress is less for tests performed with lesser strain rates; these results are consistent with those of Sallfors (1975) and Leroueil et al. (1985) for soft clay.

Additional simulations were performed for various non-hydrostatic strain-rate controlled loading conditions (K_0 compression, undrained triaxial compression, drained triaxial compression). The 1-dimensional model parameters are the same as for the previous simulations, but 3-dimensional model parameters must be added and initial conditions are different as shown in Table 5.4. Stress-strain curves and stress paths are shown in Figures 5.7 through 5.9. As for the hydrostatic compression loading conditions, inelastic deformation accumulates under lesser stress states when lesser strain rates are applied.

For a simulation in which the strain rate is constant, the stress-strain behavior and stress path behavior follow one of the constant-strain-rate backbone curves shown in Figures 5.5 or 5.7 to 5.9. However, when the applied strain rate or stress rate changes, the stress-strain behavior and/or stress path behavior of a material deviates from its previous constant-strain-rate curve. Simulations were performed in which the applied strain rate undergoes step changes as

compression proceeds. Results from these simulations are shown in Figures 5.10 to 5.13 for various loading conditions. Inspection of Figure 5.10 reveals that under hydrostatic loading conditions, the stress-strain behavior of a material moves from one constant-strain-rate backbone curve to another when the applied strain-rate is changed. In contrast, the stress-strain behavior and stress path behavior of a material under K_0 compression, undrained triaxial compression, or drained triaxial compression loading conditions deviates from the corresponding constant-strain-rate backbone curves, as shown in Figures 5.11 to 5.13 (although the constant-strain-rate backbone curves do provide good approximations of the model behavior). Therefore, material behavior for these loading paths cannot be normalized to that for constant-strain-rate tests using only applied strain rate or stress rate.

A significant aspect of the various stress-strain curves and stress paths shown in Figures 5.11 to 5.13 is that the available shear strength decreases as strain rate decreases. This behavior is consistent with the strain-rate controlled triaxial compression test results of Hayano et al. (2001) for soft rock, Tatsuoka et al. (1999) for sand, and Graham et al. (1983) for clay.

MODEL VERIFICATION

The constant-rate-of strain (CRS) performed as part of the simulations in the previous section may be analyzed with respect to rate-dependent behavior as follows. For each test, the apparent yield stress may be obtained from each stress-strain curve at the apparent break in slope between elastic and elasto-viscoplastic behavior. For example, the data of Figure 5.5 is reproduced in Figure 5.14, additionally marking the point at which the total stress rate decreases to one-tenth of the elastic stress rate. At this point, from equation (5.10), the stress rate for the one-dimensional model becomes:

$$\dot{p} = 0.1K\dot{\varepsilon}_v \tag{5.73}$$

which may be rearranged using equations (5.5) and (5.10) as follows:

$$\dot{\varepsilon}_v = \frac{9\psi}{1+e}\left(\frac{p}{p_c}\right)^{\frac{\lambda-\kappa}{\psi}} \tag{5.74}$$

The yield stress may be expressed as a function of the strain rate by rearranging equation (5.74) and then taking the logarithm of the equation:

$$\ln(p) = \frac{\psi}{\lambda - \kappa}\ln(\dot{\varepsilon}_v) + \left[\frac{\psi}{\lambda - \kappa}\ln\left(\frac{1+e}{9\psi}\right) + \ln(p_c)\right] \tag{5.75}$$

It is apparent that equation (5.75) describes a linear relationship between yield stress and strain rate in log-log space. In log-log space, the slope of the best-fit line is equal to $\psi/(\lambda-\kappa)$. The data of Figure (5.5) obeys this relationship, as shown in Figure 5.15. For the hydrostatic compression simulation results shown in Figure 5.15, the slope is equal to 0.036, which is equal to $\psi/(\lambda-\kappa)$ for the parameter values selected for the simulations: $\psi = 0.01$, $\lambda = 0.30$, and $\kappa \approx 0.02$ for the conditions of interest ($K = 100000$ kPa, $p \approx 1000$ kPa, $e \approx 1.0$).

A similar relationship, of the following form, may be derived for the three-dimensional model and other non-hydrostatic tests:

$$\ln(p) = c_1 \frac{\psi}{\lambda - \kappa}\ln(\dot{\varepsilon}_1) + c_2 \tag{5.76}$$

For non-hydrostatic loadings, the slope of the yield stress-strain rate curve in log-log space is proportional to but not equal to $\psi/(\lambda-\kappa)$, while the intercept is also different from that shown in equation (5.75). The apparent yield stresses for simulated K_0 compression loadings and drained triaxial compression loadings (see Figures 5.7 and 5.9) are also shown in Figure 5.15. In each case, it is clear that the trend between yield stress and strain rate is linear in log-log space.

Several CRS tests were performed on chalk samples obtained from the Lixhe chalk outcrop and saturated with various fluids as part of the European PASACHALK project (PASACHALK, 2004). For each test, as for the simulations above, the apparent yield stress was plotted as a function of strain rate. The data (PASACHALK, 2004) is shown in Figure 5.16. It is clear that for Lixhe chalk, the trend between yield stress and strain rate is linear in log-log space. This trend in real data provides verification that the rate-dependent model describes the rate-dependent behavior of chalk very well over a wide range of loading rates.

It is apparent that the trendlines shown in Figure 5.16 exhibit different slopes and intercepts for dry chalk, oil-saturated chalk, and water-saturated chalk. The subject of pore-fluid effects on mechanical behavior of chalk is addressed in Chapter 8.

COMPARISON WITH EXPERIMENTAL RESULTS

Many rate-dependent constitutive creep tests have been performed in the laboratory, under various stress- and strain-controlled conditions, to determine the creep behavior of North Sea chalk. The rate-dependent chalk model was used to simulate several of these results for deep-sea and outcrop chalks as described in this section.

Four simulations illustrate the performance of the model under loadings described by creep case 2 above (*i.e.*, σ_1-constant creep under K_0 conditions); under these conditions, the axial strain increases and the radial stress changes as creep progresses. Two simulations apply to water-saturated Stevns Klint outcrop chalk, and two simulations apply to water-saturated South Arne field chalk. Multiple creep stages were performed, under different stress conditions, during all tests.

Two creep phases were simulated for both Stevns Klint laboratory tests (Files 462 and 463). Results of the creep phases for Stevns Klint chalk are shown in Figures 5.17 and 5.18 with comparisons to the observed behavior. The best-fit values for the model parameters are given in Table 5.5. It may be seen that the model is able to closely simulate the creep behavior of the Stevns Klint chalk. The simulated axial strain history matches the observed axial strain history very closely, while the simulated and observed radial stress histories do not match as well. Note however that the observed radial stresses remain nearly constant during creep; therefore, the slight oscillations in radial stress observed during creep appear magnified in Figures 5.17(b) and 5.18(b) and may be anomalies from true creep behavior.

Two creep phases were simulated for one South Arne laboratory result (File 400), while five creep phases were simulated for the other result (File 412). The first of six creep phases in File 412 was not simulated, because the pore fluid was changed from oil to water during this phase; the effects of pore fluid on the constitutive model are not introduced until later. See Chapter 8 for creep results and simulations with various combinations of pore fluids. Results of the creep phases for South Arne chalk are shown in Figures 5.19 and 5.20 with comparisons to the observed behavior. The best-fit values for the model parameters are given in Table 5.6. It is apparent that the model is able to closely simulate the creep behavior of South Arne chalk. The simulated axial strain history and radial stress history match the observed axial strain history and radial stress history closely.

Three additional simulations illustrate the behavior of the model under variable loading rate conditions. Several isotropic compression tests with various stress rate-controlled stages, including creep stages, were performed on Lixhe chalk samples as part of the PASACHALK project to examine the effect of loading rates on mechanical behavior. These different stress rates imposed include a "fast" stress rate ($\dot{p} = 3.3e-3$ MPa/s), a "slow" stress rate ($\dot{p} = 5.5e-5$ MPa/s), and creep. The tests were performed under the following conditions:

- Test T2: slow stress rate, creep 1, slow stress rate, creep 2, fast stress rate, creep 3
- Test T4: slow stress rate, fast stress rate (load-unload), creep 1
- Test T5: fast stress rate, creep 1, fast stress rate, creep 2

It should be noted that tests T4 and T5 were performed on samples with the same porosity, so differences in behavior are believed to be due only to differences in loading rate.

The simulated behavior for test T2 is shown in Figure 5.21 and compared with the observed behavior. It may be seen that the stress-strain behavior and creep behavior match the test results fairly well, although some discrepancies are apparent. The simulated and observed behavior for tests T4 and T5 are shown in Figure 5.22. It may be seen that while the samples used for these two tests are the same, their yield stresses or apparent preconsolidation stresses are different; this behavior is consistent with the behavior predicted by the rate-dependent model. For both T4 and T5, the simulated stress-strain behavior and creep behavior agrees well with the observed behavior. For all tests, the values for the required model parameters are shown in Table 5.7.

REFERENCES

Bjerrum, L. (1967). Engineering geology of Norwegian normally consolidated marine clays as related to settlements of buildings. 7th Rankine Lecture, *Geotechnique*, 17 (2), 83-117.

Borja, R.I. and Kavazanjian, E. (1985). A constitutive model for the stress-strain-time behavior of wet clays. *Geotechnique*, 35 (3), 283-298.
118.

DeGennaro, V., Delage, P., Cui, Y.-J., Schroeder, C., and Collin, F. (2003). Time-dependent behaviour of oil reservoir chalk: a multiphase approach. Soils and Foundations, 43(4), 131-147.

Desai, C.S., and Zhang, D. (1987). Viscoplastic model for geologic materials with generalized flow rule. *International Journal for Numerical and Analytical Methods in Geomechanics*, 11 (6), 603-620.

DiBenedetto, H. (1987). Modelisation du comportement des geomateriaux: application aux enrobes bitumeneux et aux bitumes. Ph.D. thesis, INPG-USTMG-ENTPE.

DiBenedetto, H., Sauzeat, C., and Geoffroy, H. (2001). Modelling viscous effects and behaviour in the small strain domains. *Proceedings of the Second International Conference on Pre-Failure Deformation Characteristics of Geomaterials, IS Torino* (ed. Jamiolkowski et al.), Balkema, 1357-1367.

DiBenedetto, H., Tatsuoka, F., and Ishihara, M. (2002). Time-dependent shear deformation characteristics of sand and their constitutive modeling. *Soils and Foundations*, 42 (2), 1-22.

Graham, J., Crooks, J.H.A., and Bell, A.L. (1983). Time effects on the stress-strain behaviour of natural soft clays. *Geotechnique*, 33 (3), 327-340.

Gutierrez, M.S. (1998). Formulation of a Basic Chalk Constitutive Model, NGI Report no. 541105-2.

Gutierrez, M.S. (1999). Modelling of Time-Dependent Chalk Behavior and Chalk-Water Interaction, NGI Report no. 541105-4.

Hayano, K., Matsumoto, M., Tatsuoka, F., and Koseki, J. (2001). Evaluation of time-dependent properties of sedimentary soft rock and their constitutive modeling. *Soils and Foundations*, 41 (2), 21-38.

Helm, D.C. (1995). Poroviscosity. *Proceedings of the Joseph F. Poland Symposium on Land Subsidence* (ed. James W. Borchers), Star Publishers, 395-405.

Homand, S., and Shao, J.F. (2000). Mechanical behavior of a porous chalk and effect of saturating fluid. Mechanics of Cohesive-Frictional Materials, 5, 583-606.

Kaliakin, V.N., and Dafalias, Y.F. (1990). Theoretical aspects of the elastoplastic-viscoplastic bounding surface model for cohesive soils. *Soils and Foundations*, 30 (3), 11-24.

Leroueil, S., Kabbaj, M., Tavenas, F., and Bouchard, R. (1985). Stress-strain-strain rate relation for the compressibility of sensitive natural clays. *Geotechnique*, 35 (2), 159-180.

PASACHALK (2004). Mechanical Behavior of Partially and Multiphase Saturated Chalks Fluid-Skeleton Interaction: Main Factor of Chalk Oil Reservoirs Compaction and Related Subsidence – Part 2, Final Report, EC Contract no. ENK6-2000-00089.

Roscoe, K.H. and Burland J.B. (1968). On the Generalized Stress-Strain Behaviour of 'Wet' Clay, in: J. Heyman and F.A. Leckie, eds., Engineering Plasticity, Cambridge University Press, Cambridge, 535-609.

Sallfors, G. (1975). Preconsolidation pressure of soft, high-plastic clays. Ph.D. thesis, Chalmers University of Technology, Gothenburg, Sweden.

Shao, J.-F., Zhu, Q.Z., and Su, K. (2003). Modeling of creep of rock materials in terms of material degradation. Computers and Geotechnics, 30, 549-555.

Sloan, S.W. (1987). Substepping schemes for the numerical integration of elastoplastic stress-strain relations. *International Journal for Numerical Methods in Engineering*, 24, 893-911.

Stolle, D.F.E., Vermeer, P.A., and Bonnier, P.G. (1999). Time integration of a constitutive law for soft clays. *Communications in Numerical Methods in Engineering*, 15, 603-609.

Tatsuoka, F., Santucci deMagistris, F., Momoya, Y., and Maruyama, N. (1999). Isotach behaviour of geomaterials and its modeling. *Proceedings of the Second International Conference on Pre-Failure Deformation characteristics of Geomaterials, IS Torino '99* (ed. Jamiolkowski et al.), Balkema, 491-499.

Tatsuoka, F., Santucci deMagistris, F., Hayano, K., Momoya, Y., and Koseki, J. (2000). Some new aspects of time effects on the stress-strain behaviour of stiff geomaterials. Keynote lecture, *The Geotechnics of Hard Soils-Soft Rocks, Proceedings of the Second International Conference on Hard Soils and Soft Rocks, Napoli 1998* (ed. Evangelista and Picarelli), Balkema, 1285-1371.

Taylor, D.W. (1948). Fundamentals of Soil Mechanics. New York, John Wiley and Sons, 700 p.

Vaid, Y.P., and Campanella, R.G. (1977). Time-dependent behaviour of undisturbed clay. *ASCE Journal of the Geotechnical Engineering Division*, 103 (7), 693-709.

William, K.J. and Warnke, E.P. (1975). Constitutive model for the triaxial behavior of concrete, ISMES Seminar on Concrete Structures Subjected to Triaxial Stress, Bergamo, Italy, 1-30.

Wood, D.M. (1990). Soil Behaviour and Critical State Soil Mechanics. Cambridge, Cambridge University Press, 462 p.

Yin, J.-H., and Graham, J. (1989). Viscous-elastic-plastic modeling of one-dimensional time-dependent behaviour of clays. *Canadian Geotechnical Journal*, 26, 199-209.

Yin, J.-H., and Graham, J. (1994). Equivalent times and vone-dimensional elastic visco-plastic modeling of time-dependent stress-strain behaviour of clays. *Canadian Geotechnical Journal*, 31, 42-52.

Yin, J.-H., and Graham, J. (1999). Elastic viscoplastic modeling of time-dependent stress-strain behaviour of soils. *Canadian Geotechnical Journal*, 36, 736-745.

Yin, J.-H., Zhu, J.-G., and Graham, J. (2002). A new elastic viscoplastic model for time-dependent behaviour of normally and overconsolidated clays: theory and verification. *Canadian Geotechnical Journal*, 39, 157-173.

Zienkiewicz, O.C., and Cormeau, I.C. (1974). Visco-plasticity, plasticity and creep in elastic solids: a unified numerical solution approach. *International Journal for Numerical and Analytical Methods in Geomechanics*, 8 (2), 821-845.

Table 5.1. Material property values and initial conditions for the comparison of one-dimensional time integration methods.

Parameter	Value
Reference compression coefficient, λ_0	0.30
Bulk modulus, K (kPa)	100000
Anchor for virgin compression curve at p = 1 kPa, N	3.072
Creep parameter, ψ	0.01
Minimum volumetric age, $t_{v,\min}$ (days)	1
Curvature parameter, A	0
Initial mean stress, p (kPa)	1000
Initial preconsolidation stress, p_c (kPa)	1000

Table 5.2. Error analysis for single-step creep simulation (Δt = 5 days).

	"Exact" solution	Explicit Euler	Explicit R-K4	Secant age	Creep solution
Volumetric strain increment, $\Delta\varepsilon_v$	0.00900	0.0250	0.0117	0.0096	0.00896
% error		178 %	30 %	6.8 %	0.4 %
Final preconsolidation stress, $p_{c,f}$(kPa)	1066.1	1178.6	1083.4	1070.7	1064.0
Δp_c (kPa)	66.1	178.6	83.4	70.7	64.0
% error		170 %	26 %	7.0 %	3.2 %

Table 5.3. Error analysis for single-step stress-relaxation simulation (Δt = 1 day).

	"Exact" solution	Explicit Euler	Explicit R-K4	Secant age	Creep solution
Final mean stress, p_f(kPa)	909.8	500	750.2	898.9	653.4
Δp (kPa)	-90.2	-500	-248.8	-101.1	-346.6
% error		454 %	177 %	12.1 %	284 %
Final preconsolidation stress, $p_{c,f}$(kPa)	1006.47	1035.7	1017.8	1007.25	1024.8
Δp_c (kPa)	6.47	35.7	17.8	7.25	24.8
% error		452 %	175 %	12.1 %	283 %

Table 5.4. Three-dimensional material parameters and initial conditions for strain-rate-controlled simulations.

	Hydrostatic compression	K_0 compression	Undrained triaxial comp.	Drained triaxial compression
Critical state parameter, M	-	1.5	1.5	1.5
William-Warnke parameter, k	-	0.65	0.65	0.65
Initial mean stress, p (kPa)	200	200	1000	500
Initial deviator stress, q (kPa)	-	0	0	0
Initial preconsol. stress, p_c (kPa)	1000	1000	1000	1000

Table 5.5. Material property values for simulations and comparison with experimental data for Stevns Klint outcrop chalk.

Parameter	File 462	File 463
Bulk modulus, K (MPa)	2500	1500
Poisson's ratio, ν	0.25	0.23
Reference compression coefficient, λ_0	0.16	0.17
Anchor for virgin compression curve at p = 1 MPa, N	1.15	1.19
Creep parameter, ψ	0.0025	0.0055
Minimum volumetric age, $t_{v,\min}$ (hours)	3	3
Curvature parameter, A	0	0
Critical state slope, M	1.09	1.08
Ellipticity parameter, R	0.70	0.69

Table 5.6. Material property values for simulations and comparison with experimental data for South Arne field chalk.

Parameter	File 400	File 412
Bulk modulus, K (MPa)	2000	1800
Poisson's ratio, ν	0.25	0.23
Reference compression coefficient, λ_0	0.15	0.17
Anchor for virgin compression curve at p = 1 MPa, N	1.15	1.19
Creep parameter, ψ	0.010	0.0035
Minimum volumetric age, $t_{v,\min}$ (hours)	1	3
Curvature parameter, A	0	0
Critical state slope, M	0.84	0.96
Ellipticity parameter, R	0.69	0.70

Table 5.7. Material property values for simulations and comparison with experimental data for Lixhe outcrop chalk.

Parameter	Test T2	Tests T4, T5
Bulk modulus, K (MPa)	2000	1500
Reference compression coefficient, λ_0	0.08	0.14
Anchor for virgin compression curve at p = 1 MPa, N	0.86	1.08
Creep parameter, ψ	0.0015	0.0084
Minimum volumetric age, $t_{v,\min}$ (hours)	0.1	0.1
Curvature parameter, A	0	0

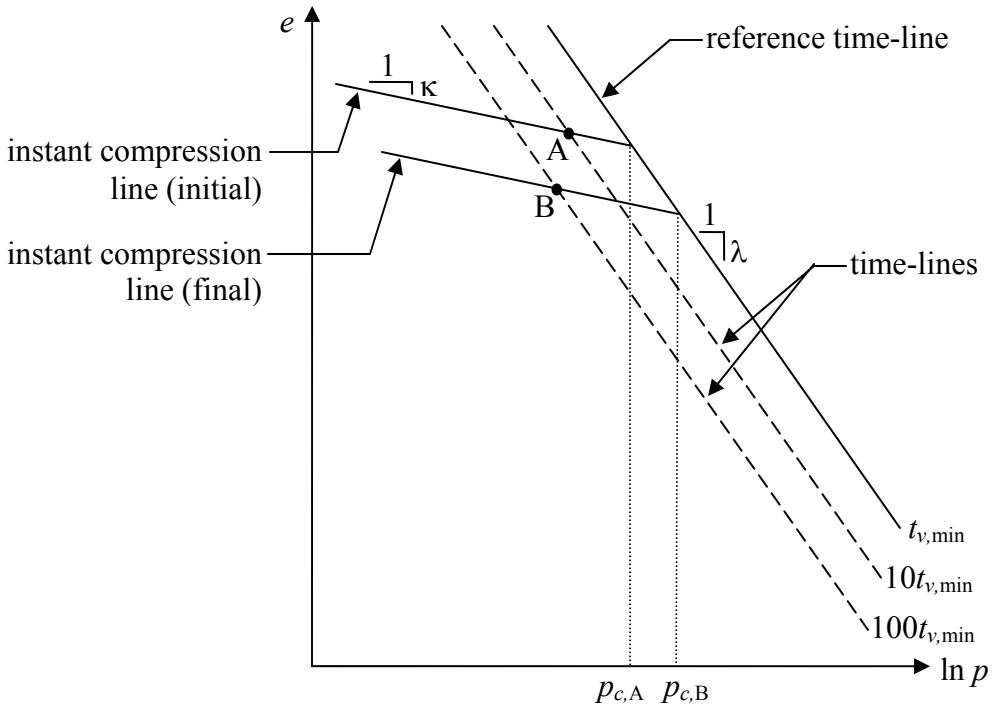

Figure 5.1. Illustration of elements in basic one-dimensional time-lines model. During loading from point A to point B, the instant compression line moves as shown and the preconsolidation stress increases from $p_{c,A}$ to $p_{c,B}$.

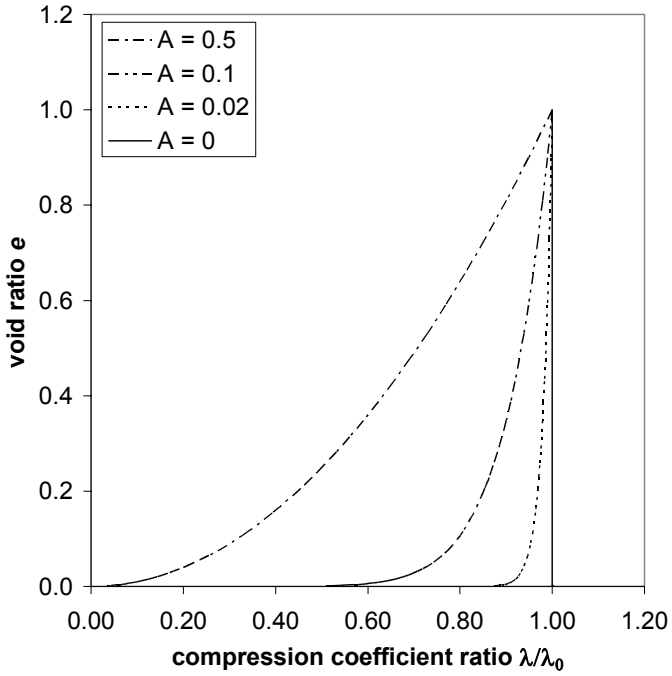

(a)

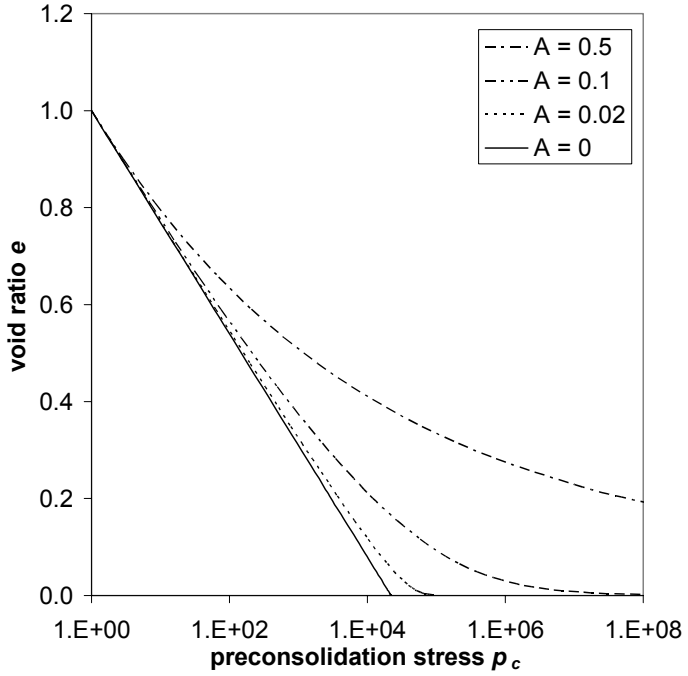

(b)

Figure 5.2. Effects of the nonlinearity parameter *A* on (a) the secant slope λ of the reference time-line, and (b) the shape of the reference time-line.

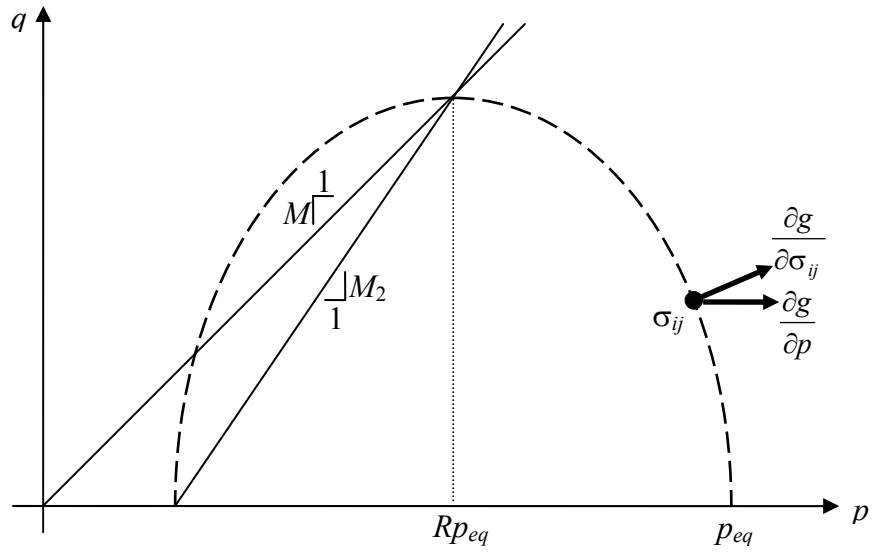

(a)

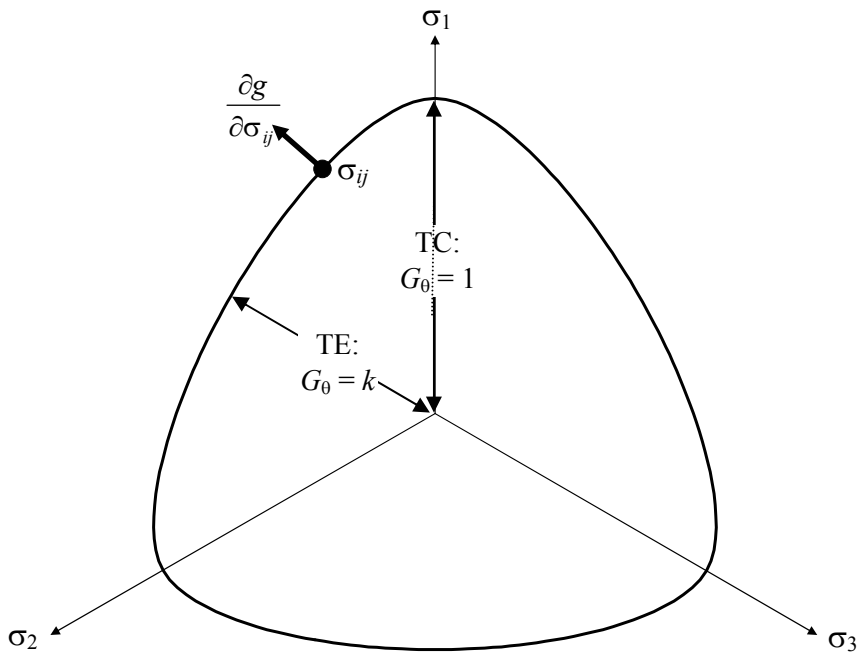

(b)

Figure 5.3. Viscoplastic potential surface for 3-dimensional rate-dependent model (a) in *p-q* space; (b) projected on the π-plane.

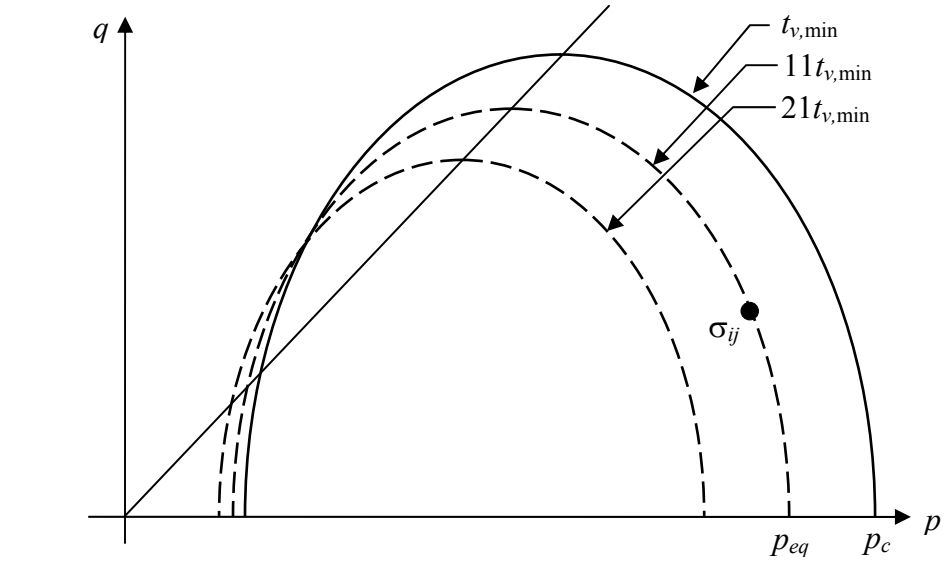

(a)

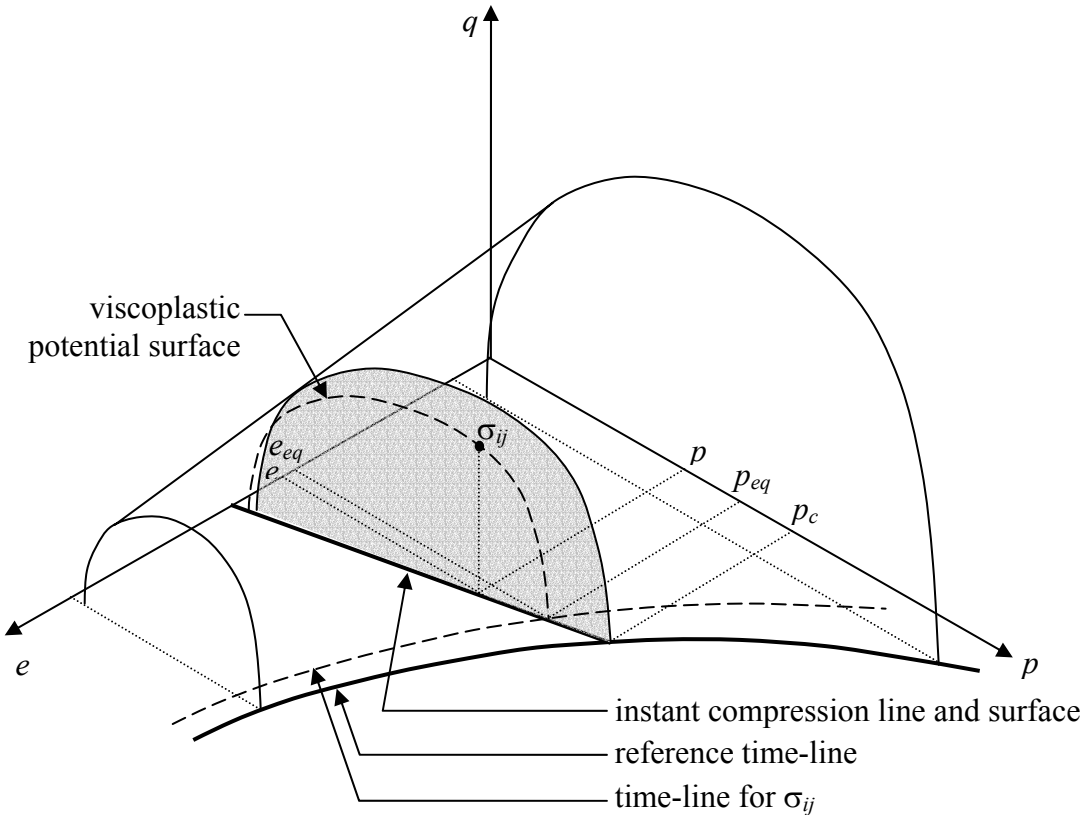

(b)

Figure 5.4. Three-dimensional time-lines model (a) in *p-q* space; (b) in *p-q-e* space. Physical meanings of parameters p_{eq} and e_{eq} and components of the rate-dependent model in *p-q-e* space. The equivalent mean stress p_{eq} and the equivalent void ratio e_{eq} are defined in the *p-e* plane, where the 1-dimensional rate-dependent model is formulated.

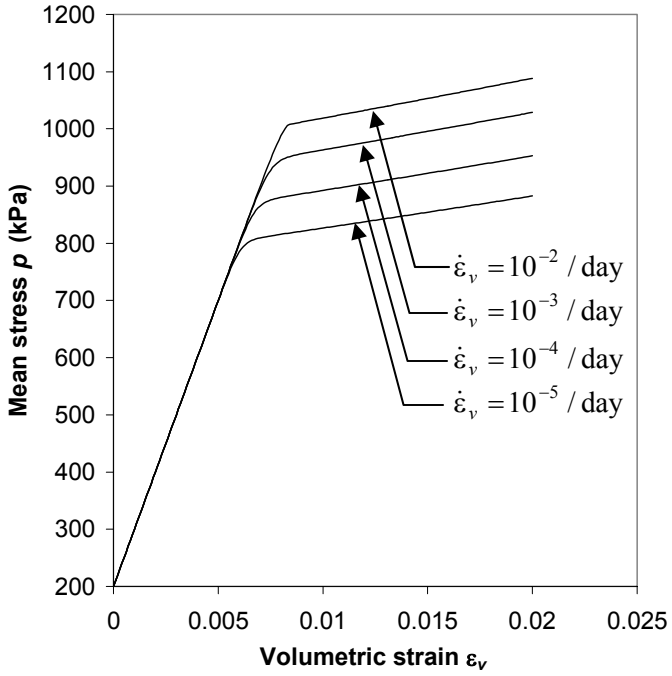

Figure 5.5. Simulation of strain-rate controlled 1-dimensional hydrostatic compression tests under various volumetric strain rates, showing effects of strain rate on stress-strain behavior.

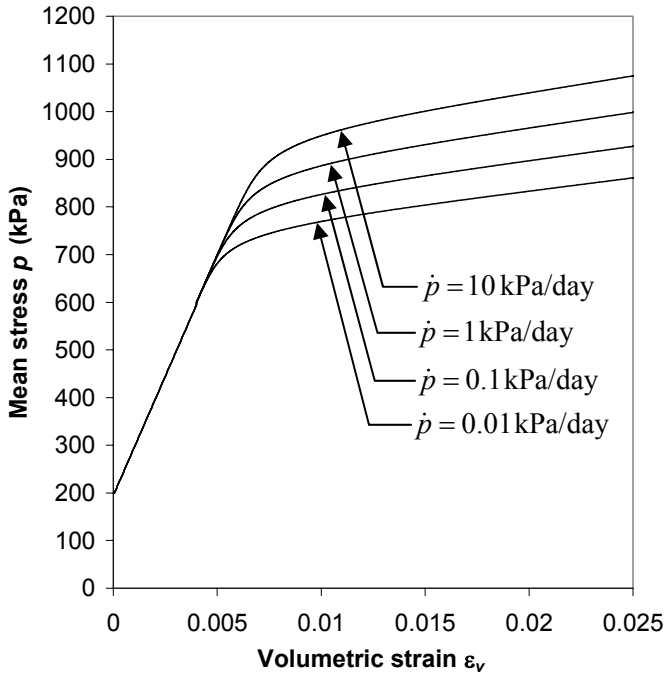

Figure 5.6. Simulation of stress-rate controlled 1-dimensional hydrostatic compression tests under various mean stress rates, showing effects of stress rate on stress-strain behavior.

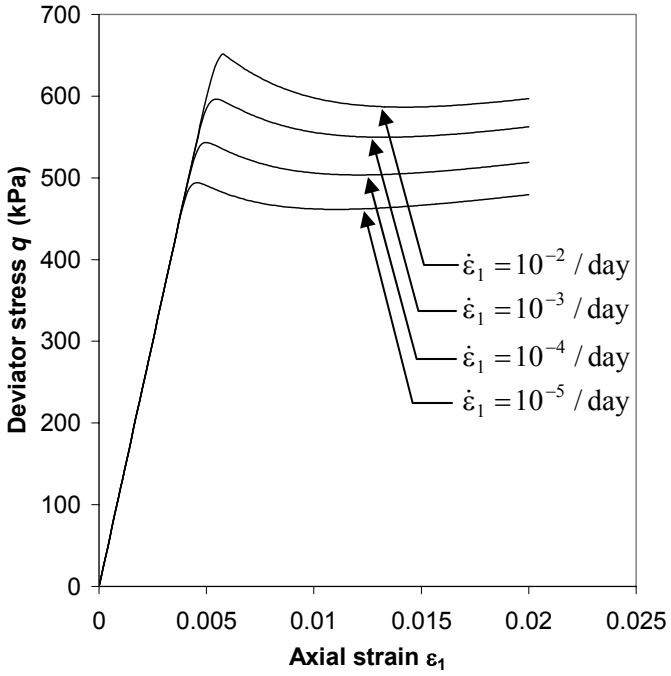

(a)

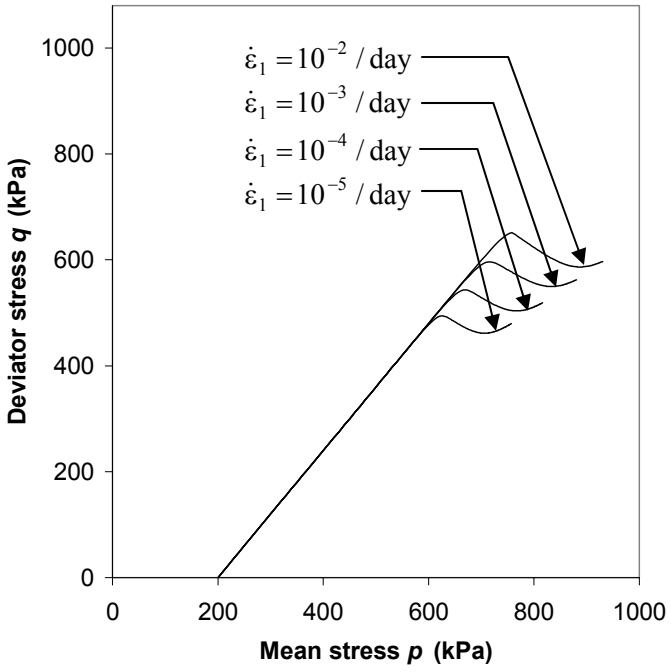

(b)

Figure 5.7. Simulation of strain-rate controlled K_0 compression tests under various axial strain rates, showing effects of strain rate on (a) stress-strain behavior and (b) stress path.

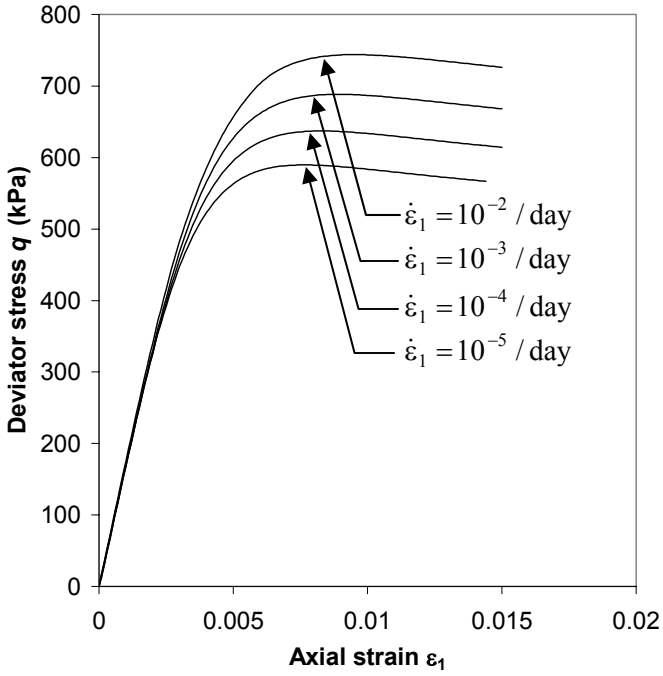

(a)

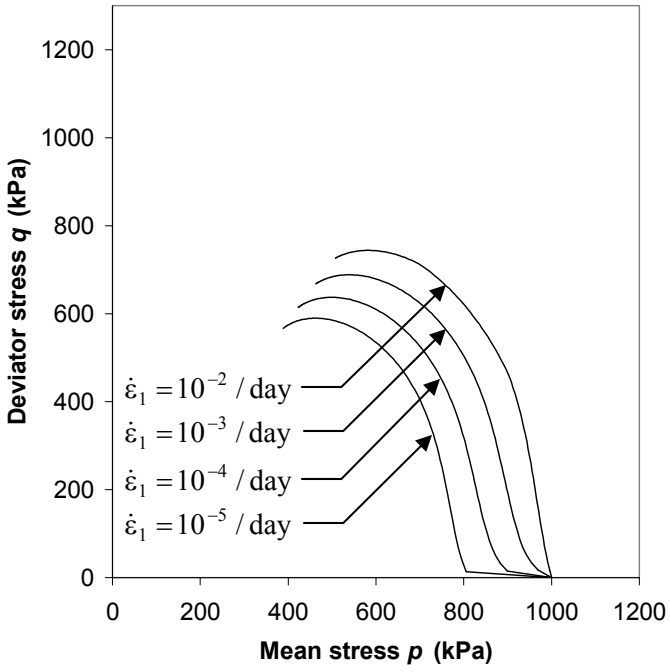

(b)

Figure 5.8. Simulation of strain-rate controlled undrained triaxial compression tests under various axial strain rates, showing effects of strain rate on (a) stress-strain behavior and (b) stress path.

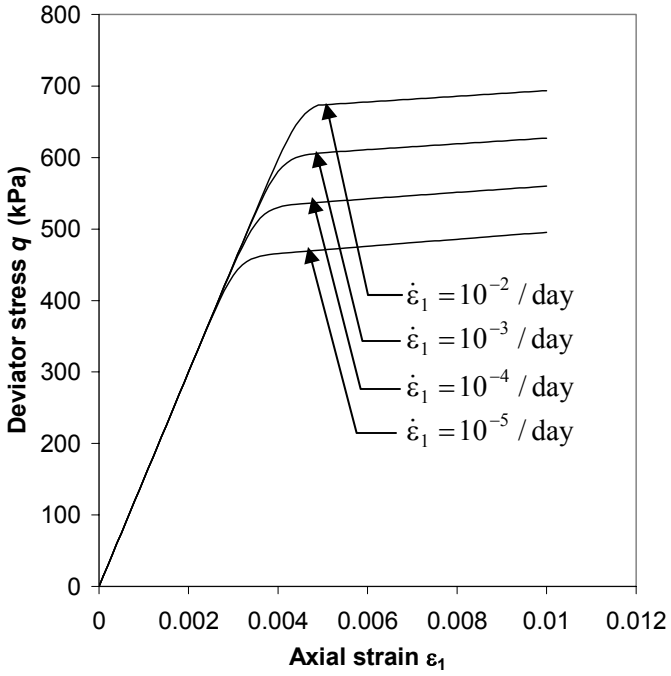

(a)

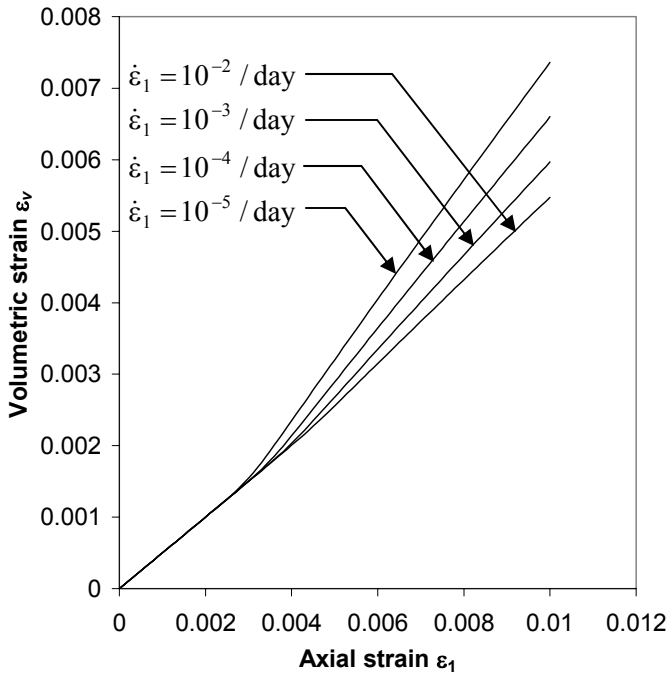

(b)

Figure 5.9. Simulation of strain-rate controlled drained triaxial compression tests under various axial strain rates, showing effects of strain rate on (a) stress-strain behavior and (b) volumetric strain behavior.

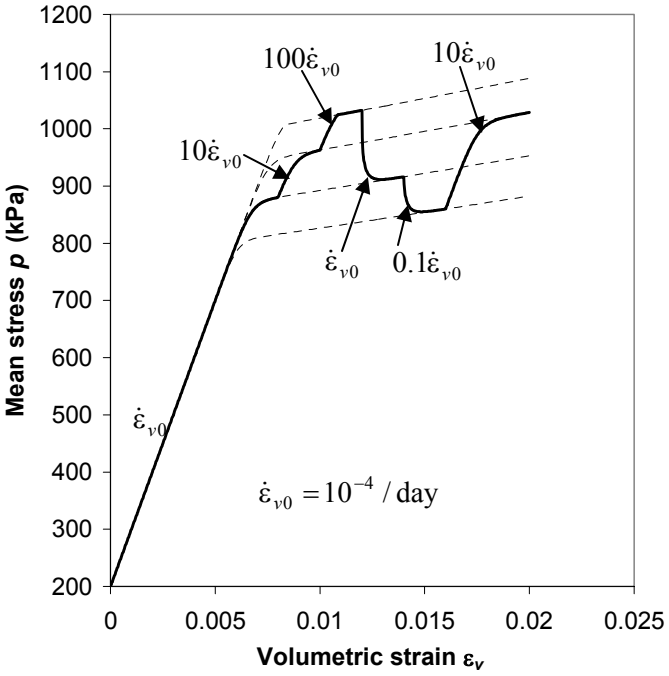

Figure 5.10. Simulation of strain-rate controlled 1-dimensional hydrostatic compression tests when the volumetric strain rate undergoes step changes. When the applied strain rate is changed, the stress-strain curve quickly approaches the backbone stress-strain curve for the new applied strain rate. The backbone curves are those shown in Figure 5.5.

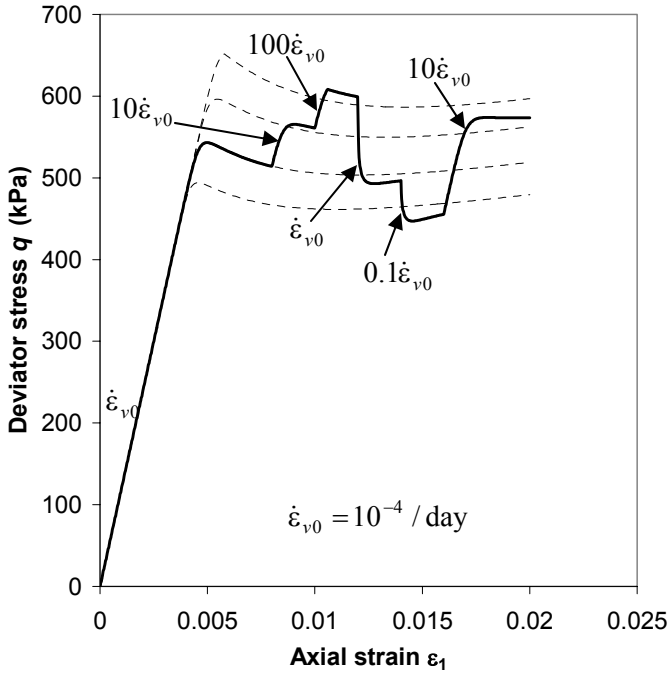

(a)

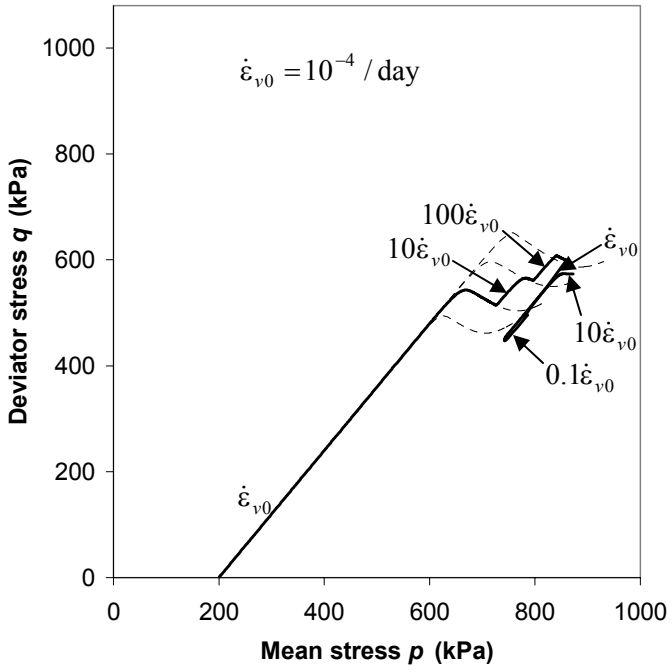

(b)

Figure 5.11. Simulation of strain-rate controlled K_0 compression tests when the axial strain rate undergoes step changes. When the applied strain rate is changed, the stress-strain curve deviates from both (a) the backbone stress-strain curve, and (b) the backbone stress path for the new applied strain rate. The backbone curves are those shown in Figure 5.7.

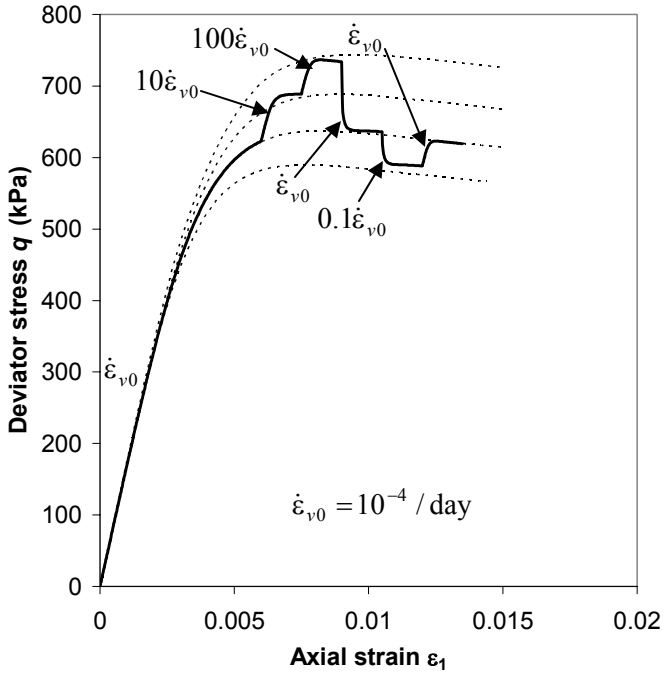

(a)

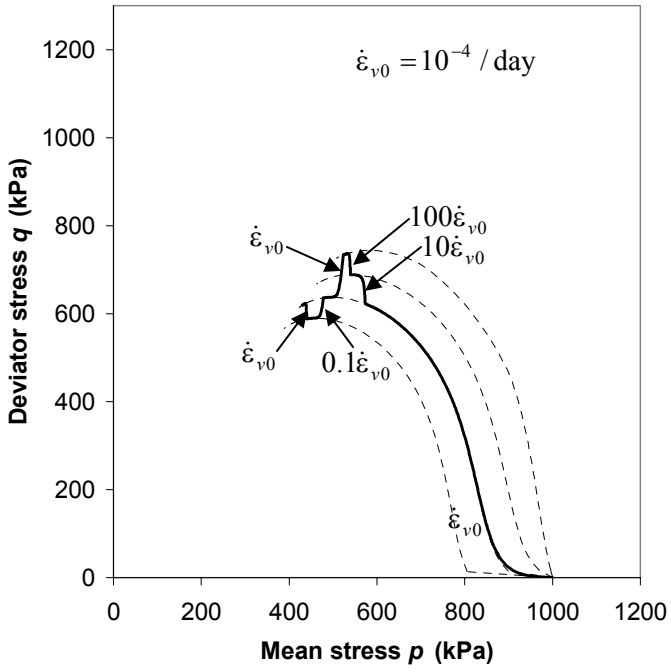

(b)

Figure 5.12. Simulation of strain-rate controlled undrained triaxial compression tests when the axial strain rate undergoes step changes. When the applied strain rate is changed, the stress-strain curve (a) deviates from the backbone stress-strain curve, but (b) follows the backbone stress path for the new applied strain rate. The backbone curves are those shown in Figure 5.8.

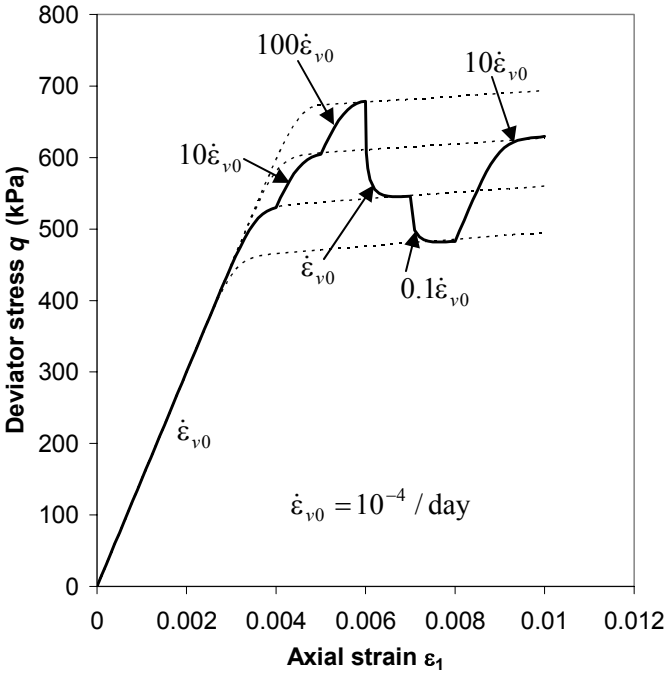

(a)

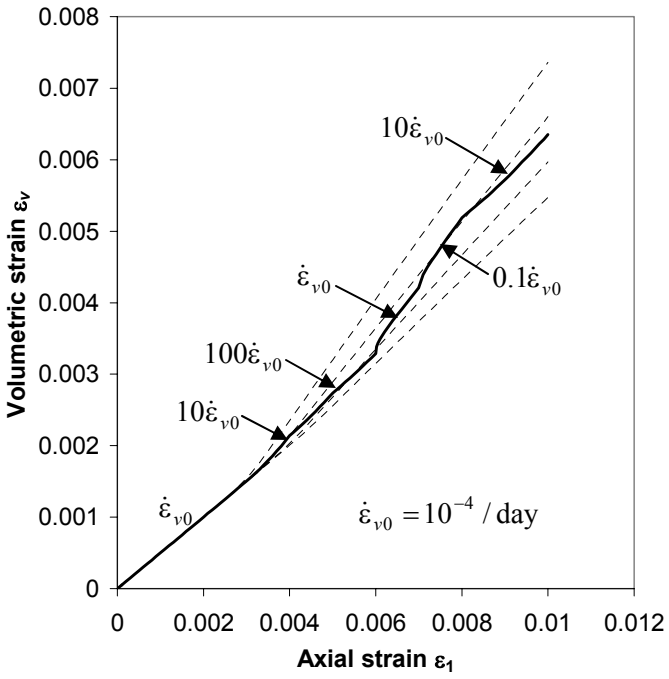

(b)

Figure 5.13. Simulation of strain-rate controlled drained triaxial compression tests when the axial strain rate undergoes step changes. When the applied strain rate is changed, the stress-strain curve (a) follows the backbone stress-strain curve, but (b) deviates from the backbone strain-strain curve for the new applied strain rate. The backbone curves are those shown in Figure 5.9.

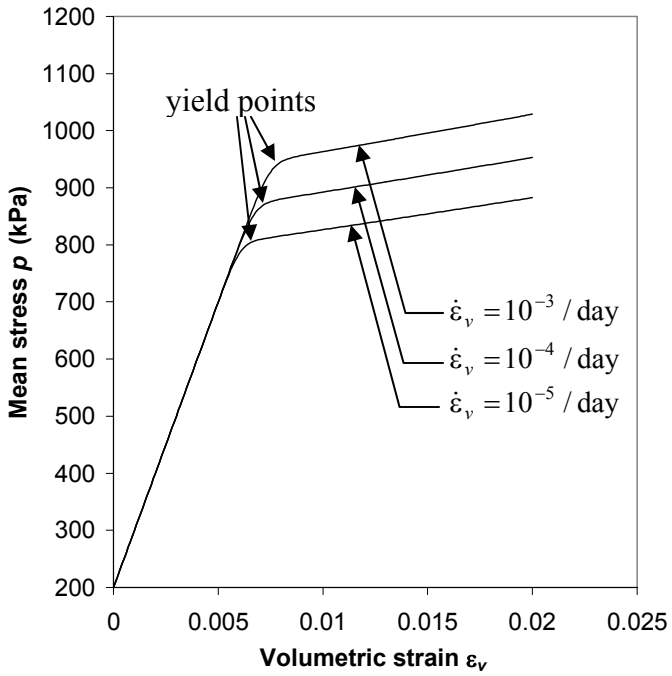

Figure 5.14. Copy of Figure 5.5: stress-strain behavior during simulated strain-rate controlled 1-dimensional hydrostatic compression tests under various volumetric strain rates, with apparent yield stresses indicated.

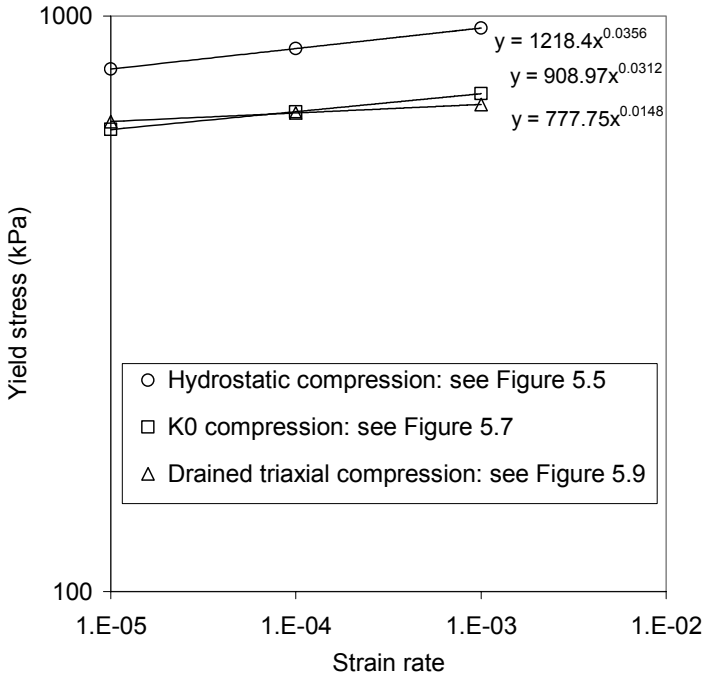

Figure 5.15. Apparent yield stress varies as a power function of applied strain for constant-rate-of-strain tests. Yield points are shown for simulated hydrostatic compression tests, K_0 compression tests, and drained triaxial compression tests; see Figures 5.5, 5.7, and 5.9.

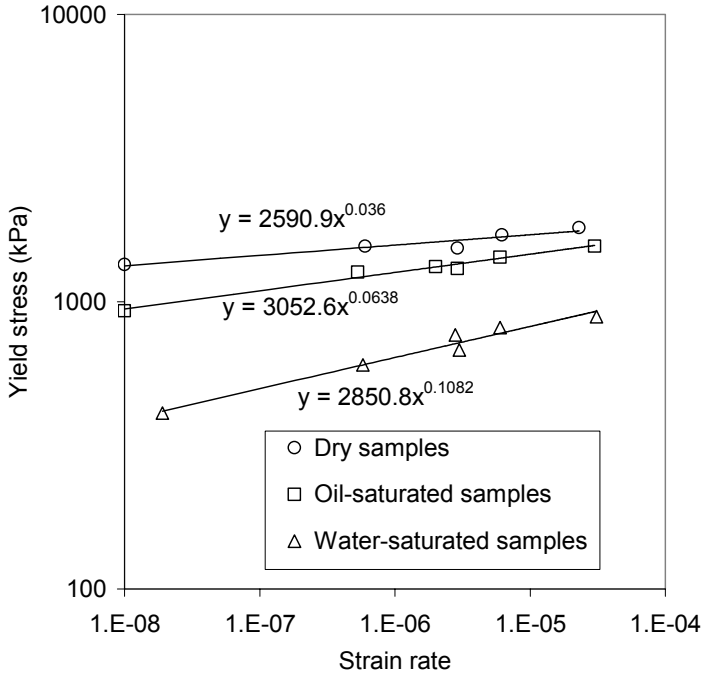

Figure 5.16. Apparent yield stress varies as a power function of applied strain for constant-rate-of-strain tests. Yield points are shown for K_0 compression tests as observed in the laboratory. Note that different trendlines exist for dry chalk, oil-saturated chalk, and water-saturated chalk (after PASACHALK, 2004).

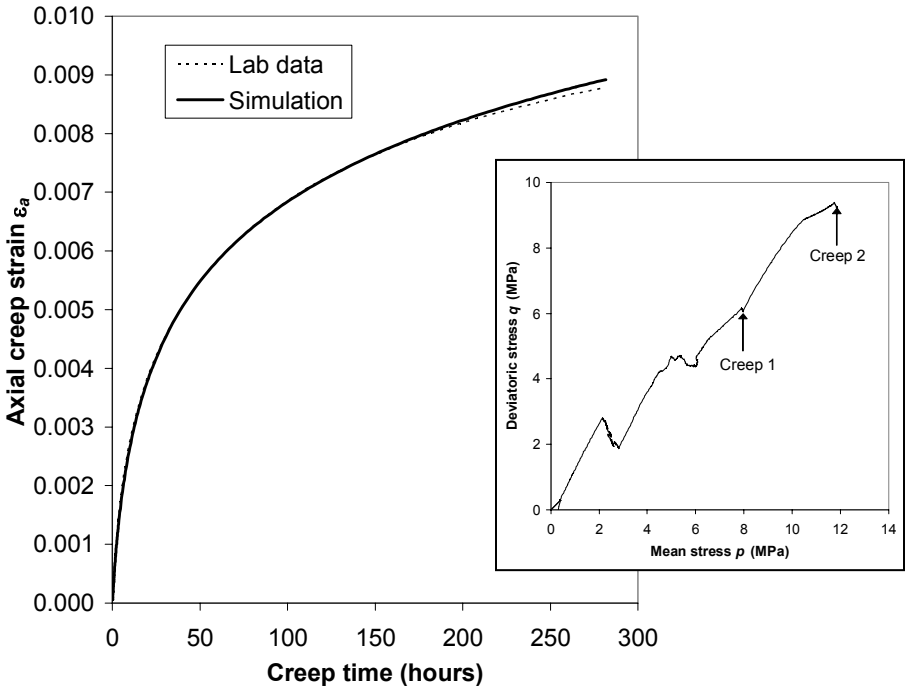

(a)

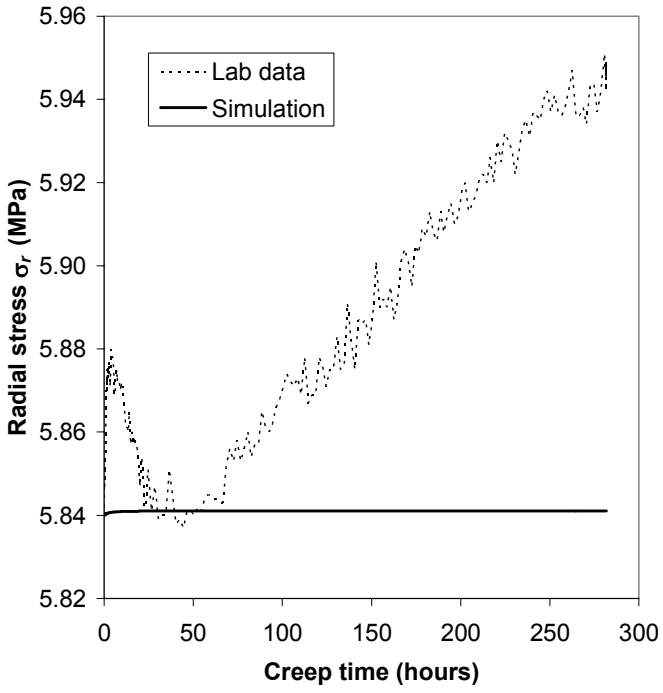

(b)

Figure 5.17. Observed and simulated data for creep phase 1 of K_0 compression test on Stevns Klint chalk (File 462): (a) axial strain history; (b) radial stress history. Stress path with creep phases is indicated in inset.

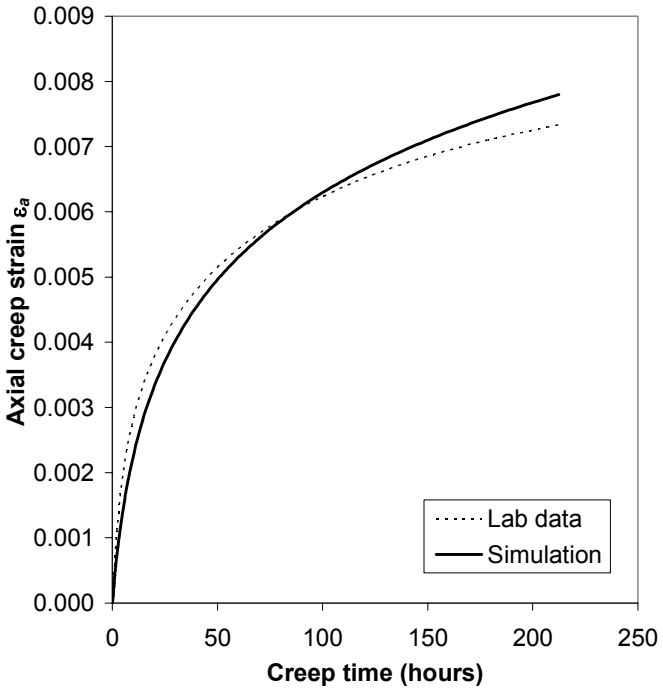

(c)

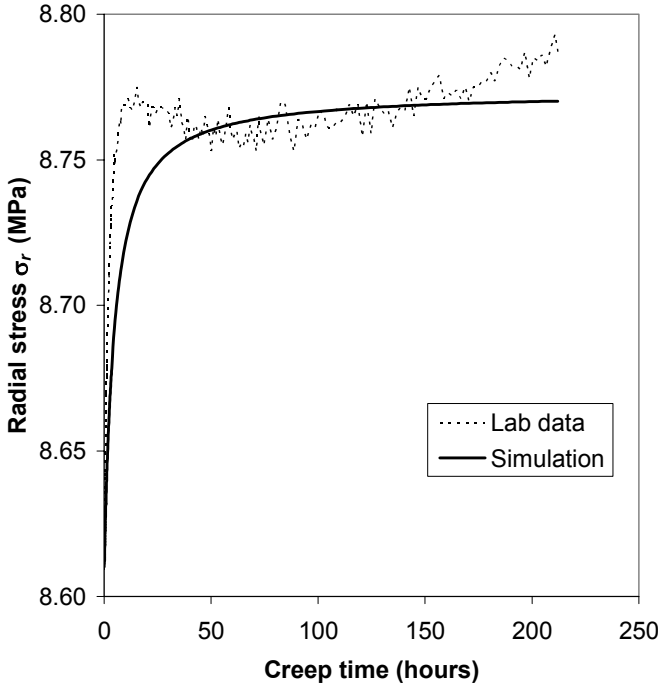

(d)

Figure 5.17 (cont.). Observed and simulated data for creep phase 2 of K_0 compression test on Stevns Klint chalk (File 462): (c) axial strain history; (d) radial stress history.

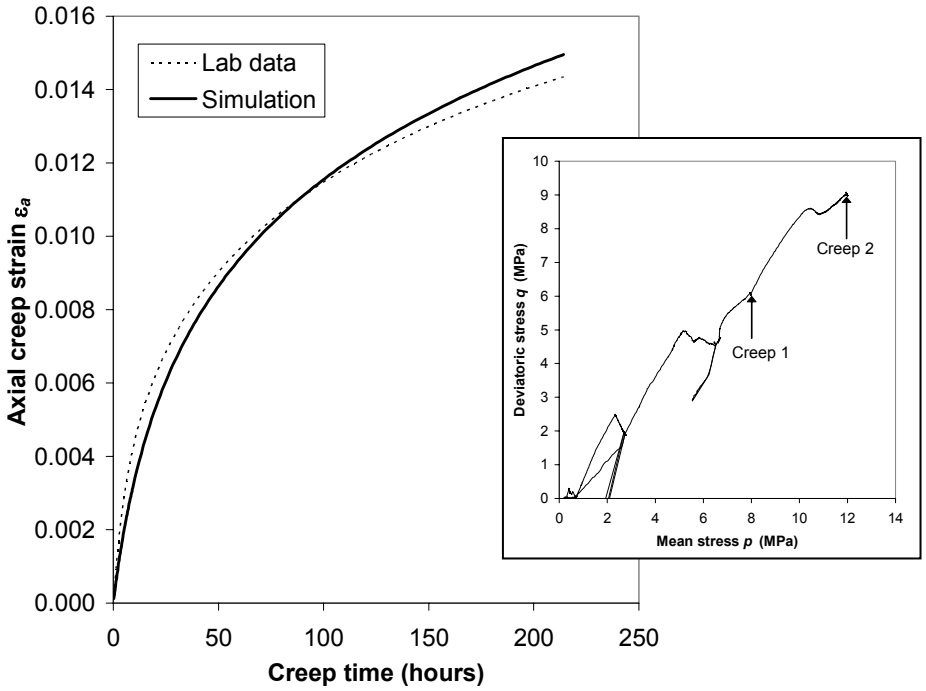

(a)

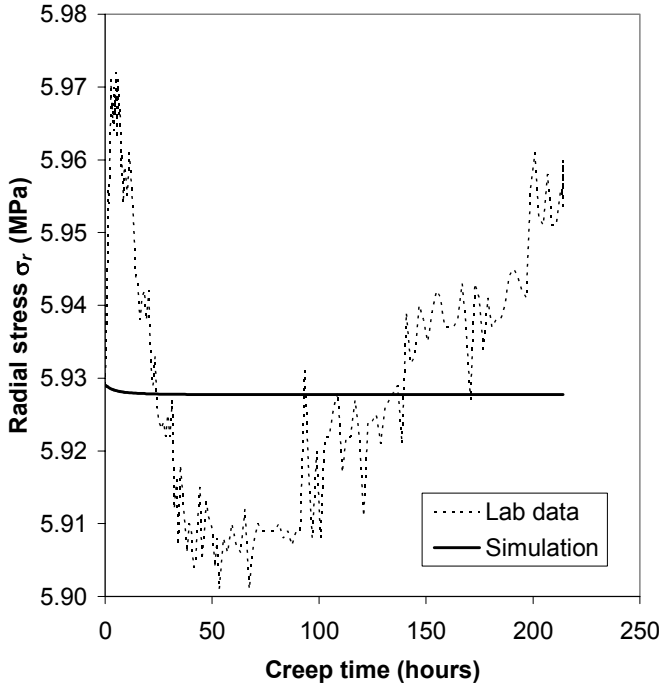

(b)

Figure 5.18. Observed and simulated data for creep phase 1 of K_0 compression test on Stevns Klint chalk (File 463): (a) axial strain history; (b) radial stress history. Stress path with creep phases is indicated in inset.

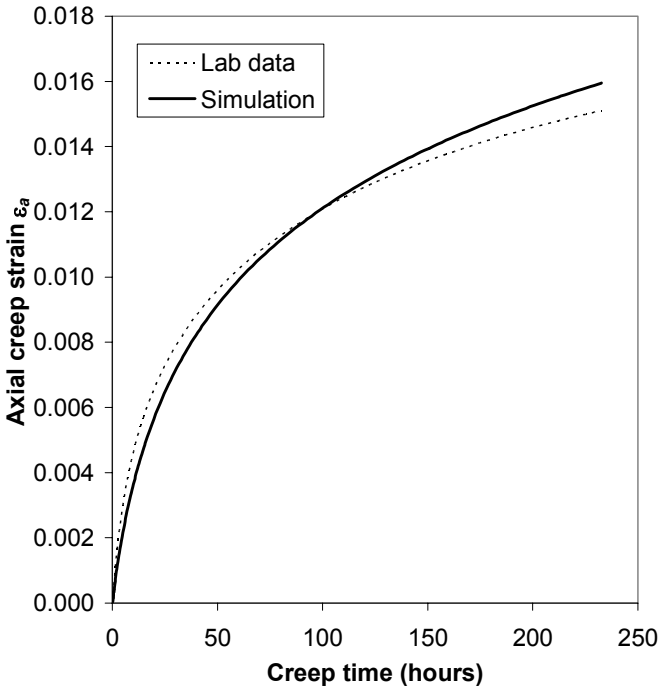

(c)

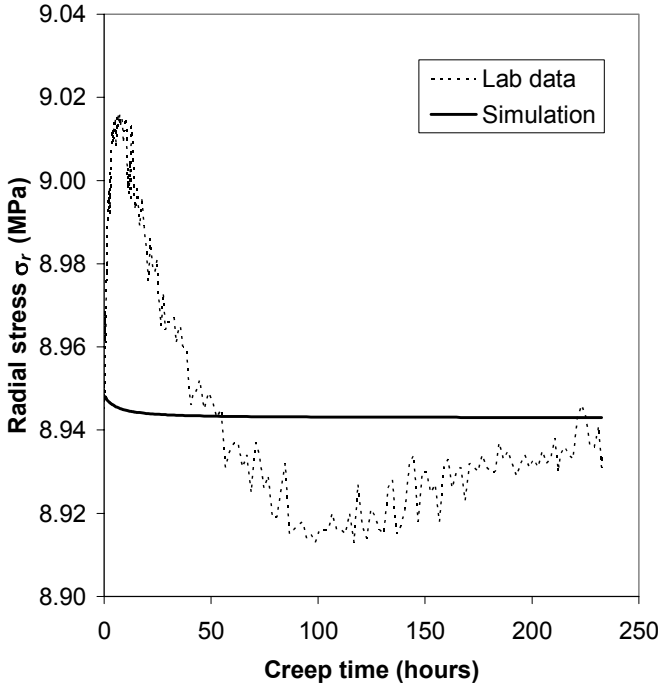

(d)

Figure 5.18 (cont.). Observed and simulated data for creep phase 2 of K_0 compression test on Stevns Klint chalk (File 463): (c) axial strain history; (d) radial stress history.

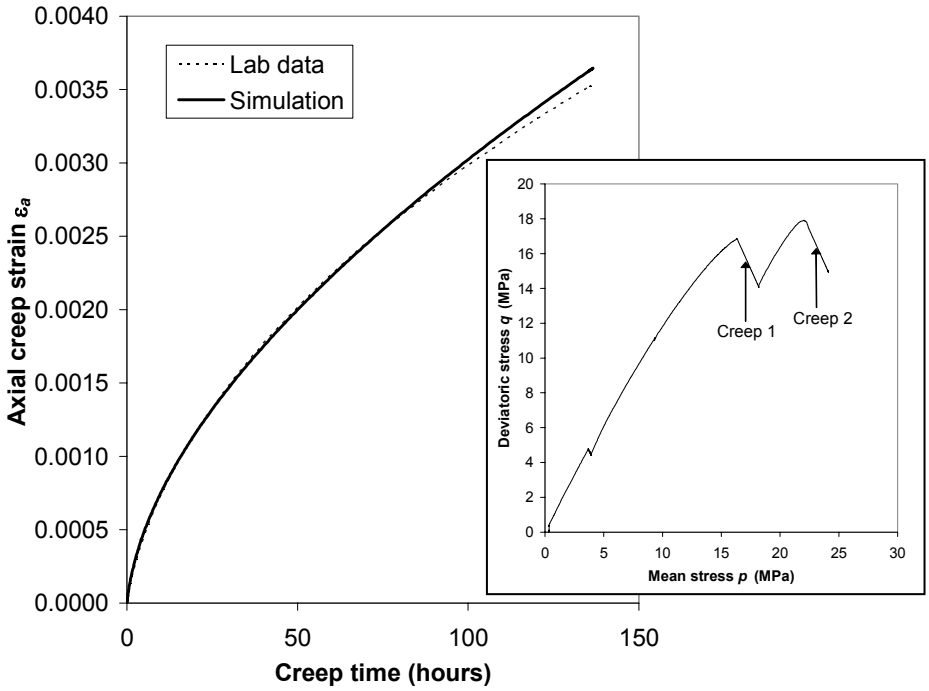

(a)

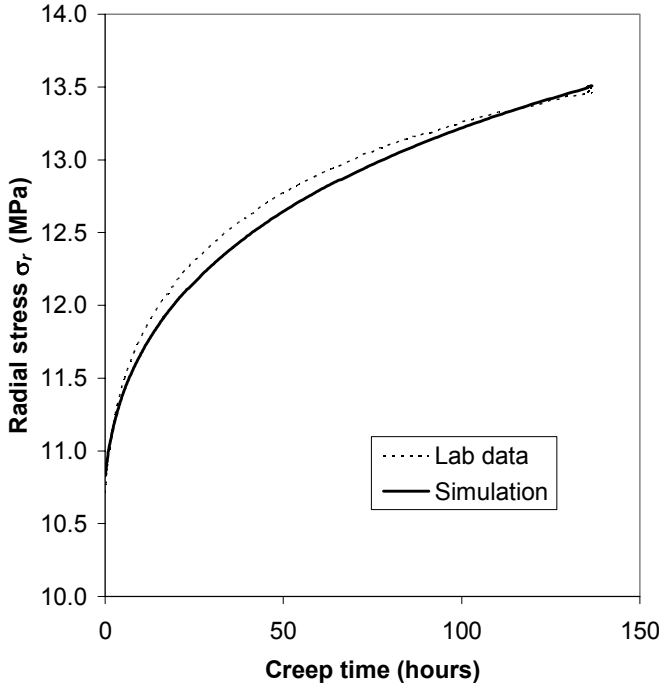

(b)

Figure 5.19. Observed and simulated data for creep phase 1 of K_0 compression test on South Arne chalk (File 400): (a) axial strain history; (b) radial stress history. Stress path with creep phases is indicated in inset.

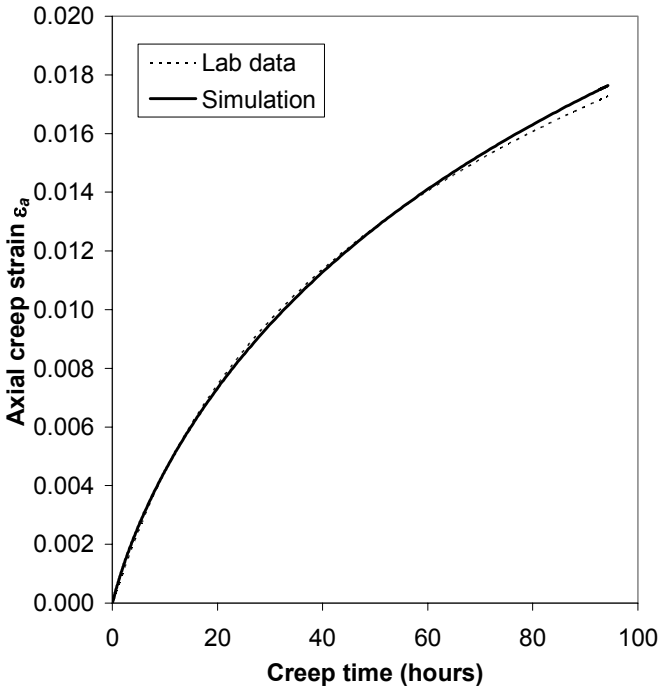

(c)

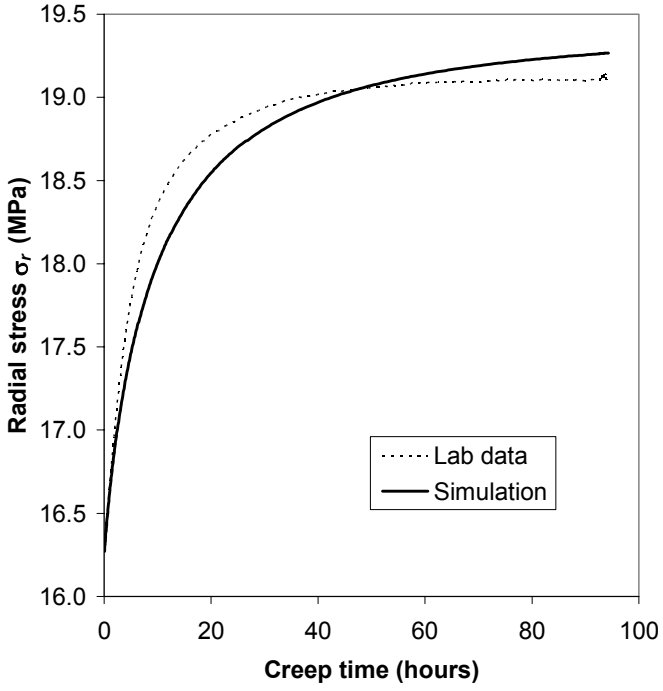

(d)

Figure 5.19 (cont.). Observed and simulated data for creep phase 2 of K_0 compression test on South Arne chalk (File 400): (c) axial strain history; (d) radial stress history.

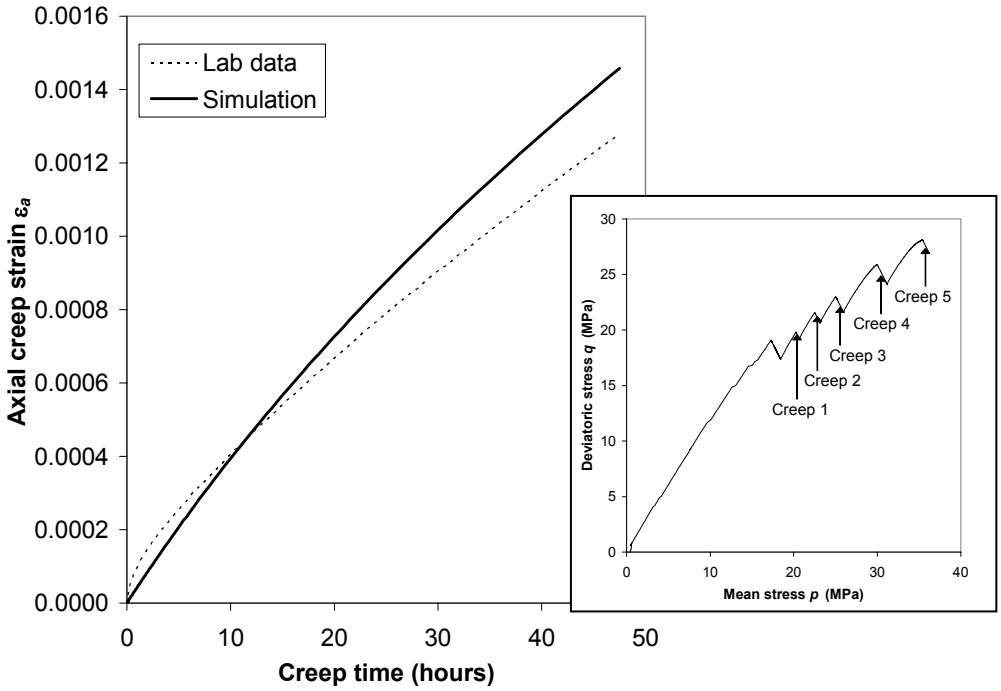

(a)

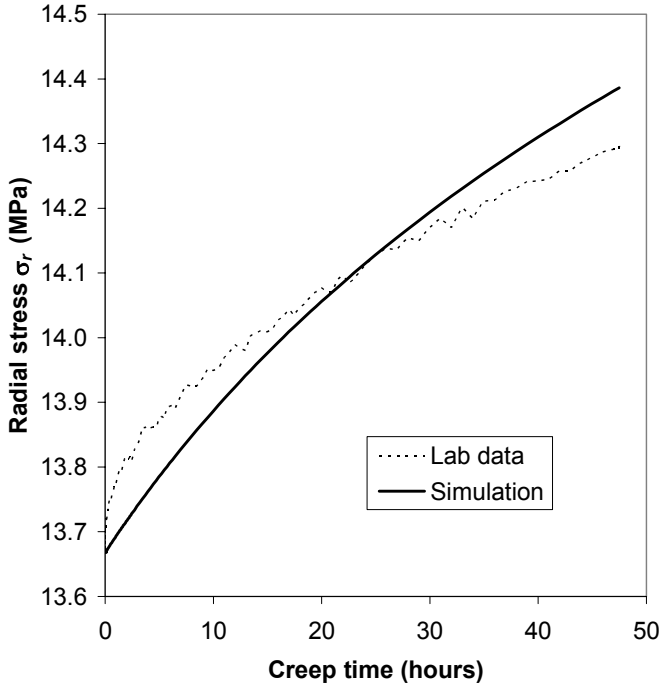

(b)

Figure 5.20. Observed and simulated data for creep phase 1 of K_0 compression test on South Arne chalk (File 412): (a) axial strain history; (b) radial stress history. Stress path with creep phases is indicated in inset.

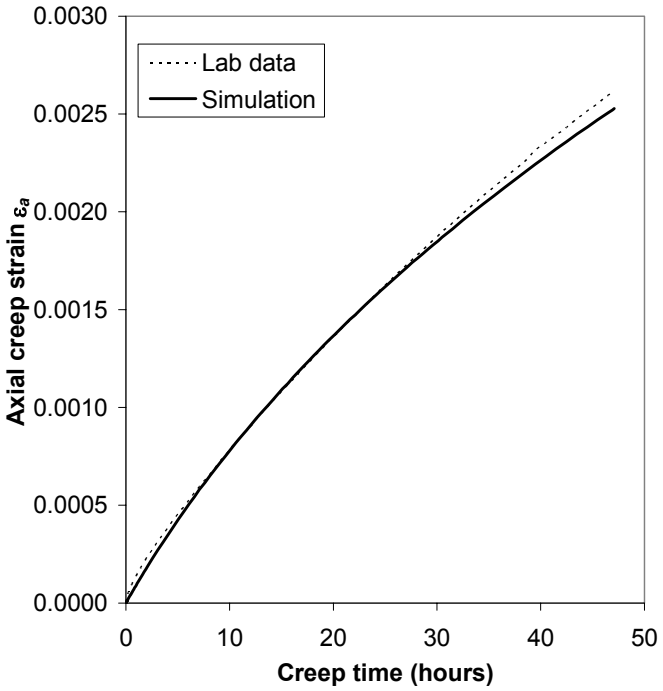

(c)

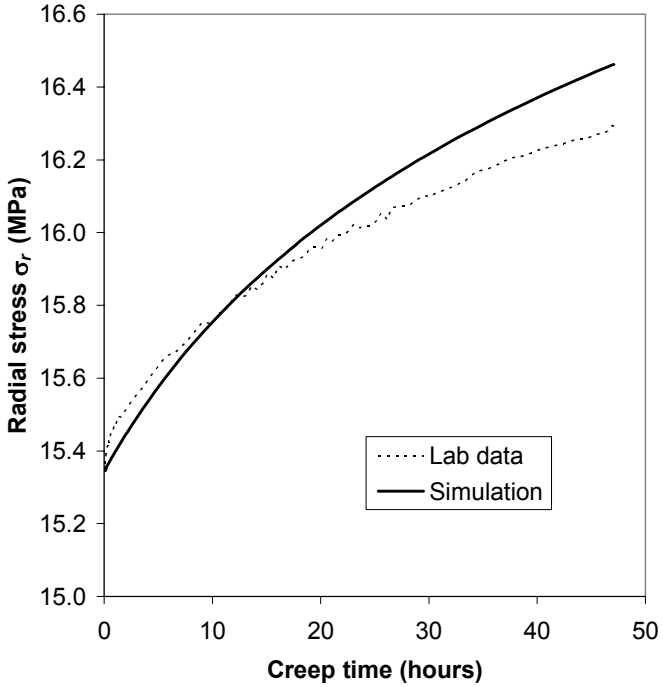

(d)

Figure 5.20 (cont.). Observed and simulated data for creep phase 2 of K_0 compression test on South Arne chalk (File 412): (c) axial strain history; (d) radial stress history.

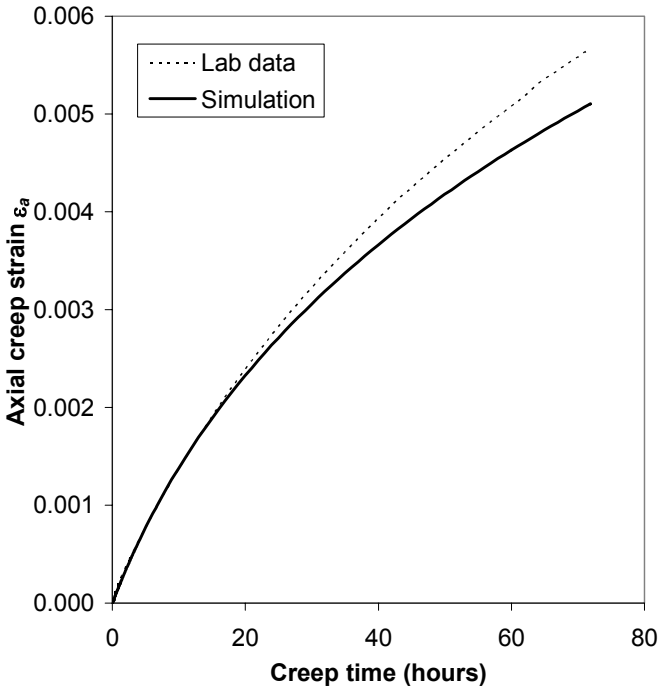

(e)

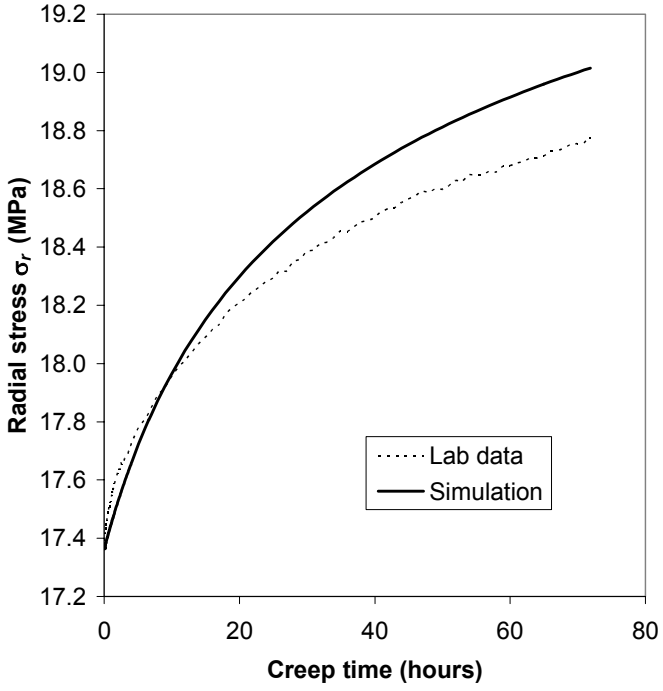

(f)

Figure 5.20 (cont.). Observed and simulated data for creep phase 3 of K_0 compression test on South Arne chalk (File 412): (e) axial strain history; (f) radial stress history.

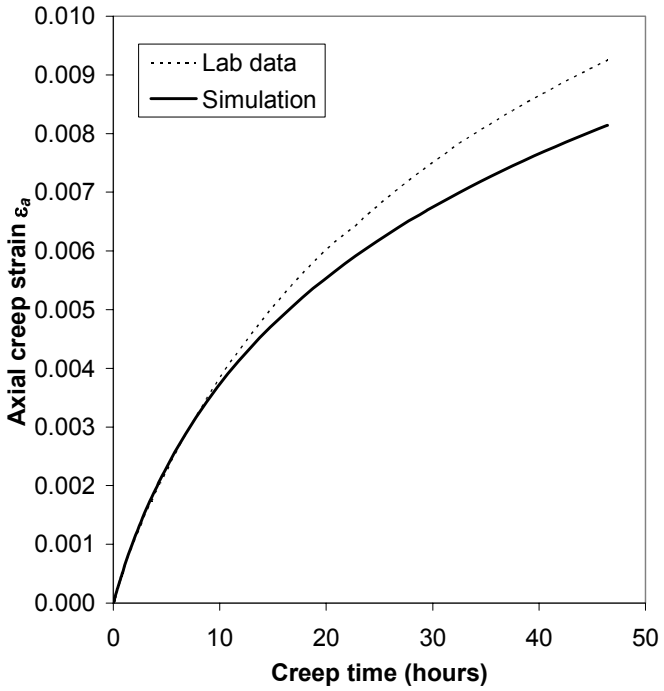

(g)

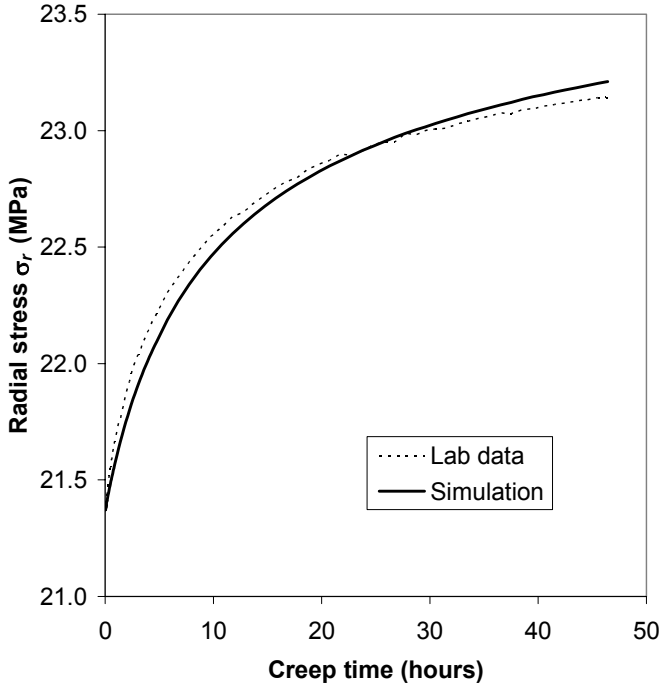

(h)

Figure 5.20 (cont.). Observed and simulated data for creep phase 4 of K_0 compression test on South Arne chalk (File 412): (g) axial strain history; (h) radial stress history.

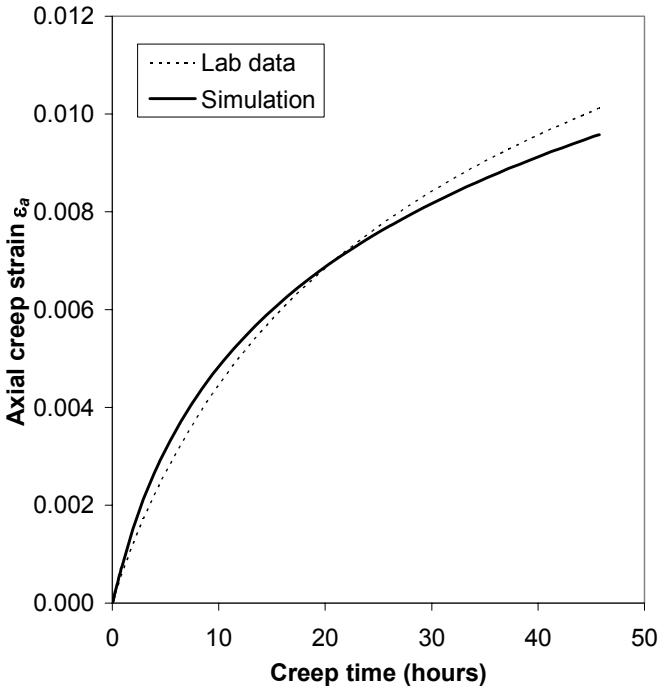

(i)

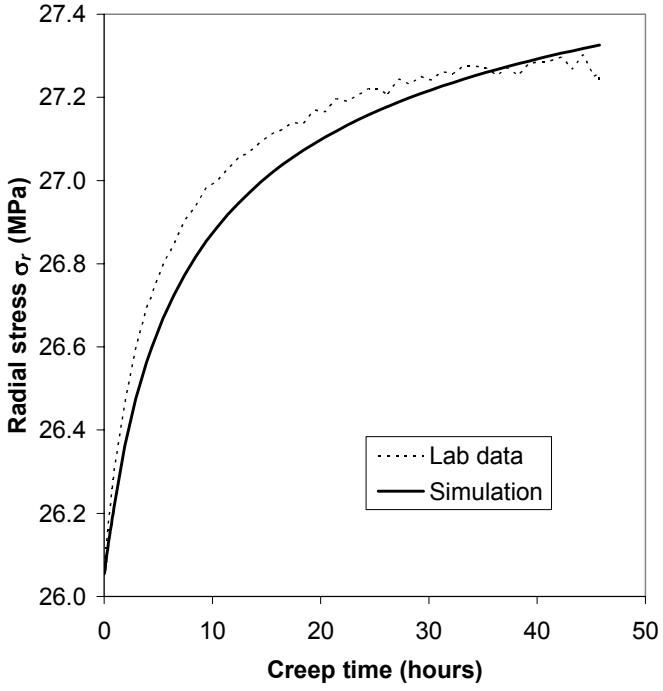

(j)

Figure 5.20 (cont.). Observed and simulated data for creep phase 5 of K_0 compression test on South Arne chalk (File 412): (i) axial strain history; (j) radial stress history.

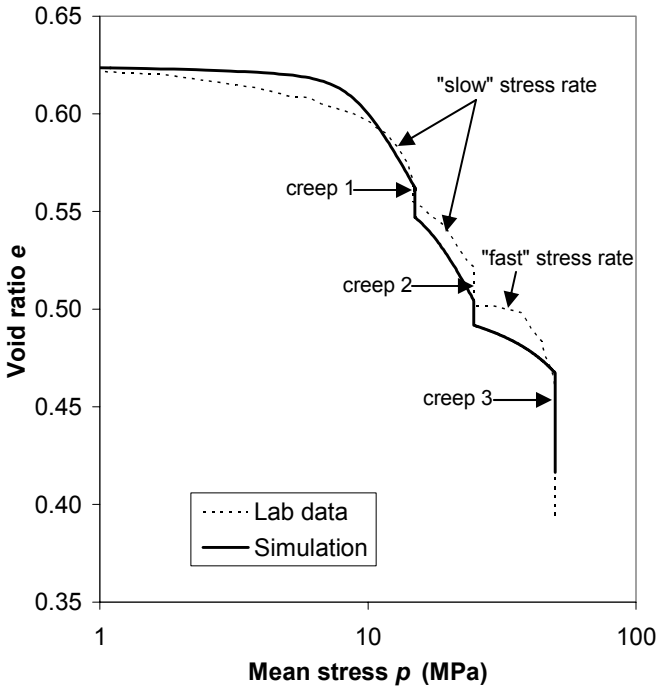

(a)

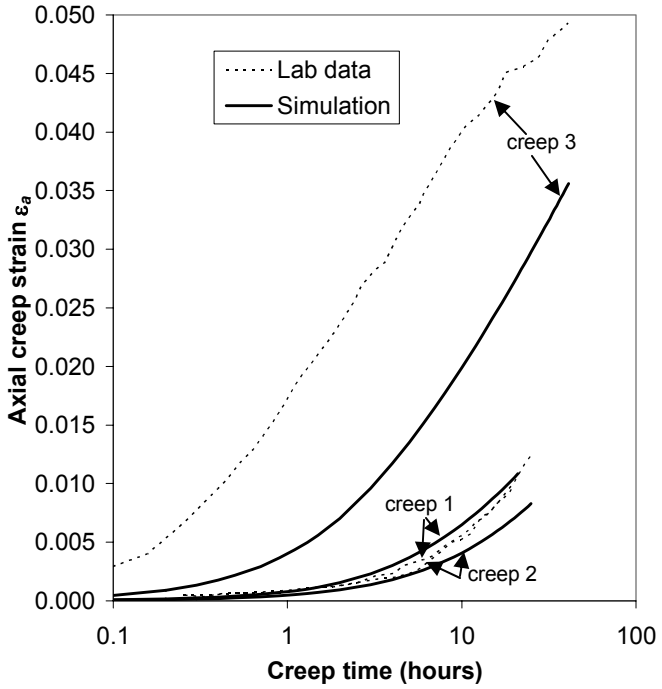

(b)

Figure 5.21. Observed and simulated data for isotropic compression test on Lixhe chalk (Test T2): (a) stress-strain behavior; (b) creep behavior. Data shown is from PASACHALK (2004).

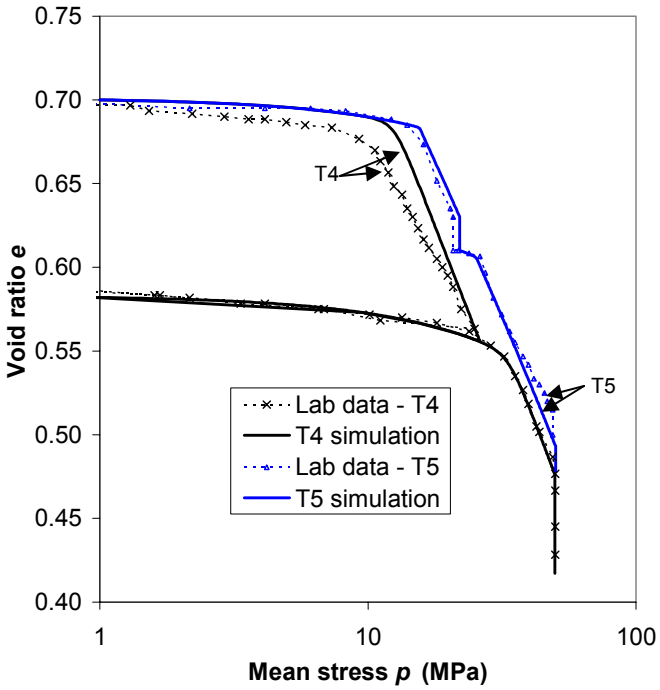

(a)

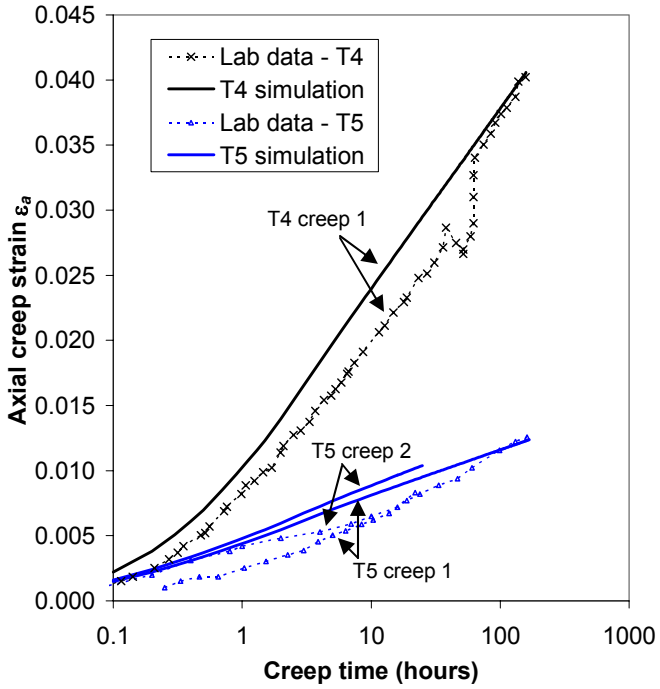

(b)

Figure 5.22. Observed and simulated data for isotropic compression tests on Lixhe chalk (Tests T4 and T5): (a) stress-strain behavior; (b) creep behavior. Data shown is from PASACHALK (2004).